



Unexpected role of metal halides in a chalcogenide glass network

Rayan Zaiter, Mohammad Kassem, Daniele Fontanari, Anton Sokolov, Takeshi Usuki, Maria Bokova, Alex C Hannon, Chris J Benmore, Fabrice Cousin, Ilya Ozheredov, et al.

► To cite this version:

Rayan Zaiter, Mohammad Kassem, Daniele Fontanari, Anton Sokolov, Takeshi Usuki, et al.. Unexpected role of metal halides in a chalcogenide glass network. *Materials & Design*, 2022, 216, pp.110547. 10.1016/j.matdes.2022.110547 . hal-03710415

HAL Id: hal-03710415

<https://hal.science/hal-03710415>

Submitted on 30 Jun 2022

HAL is a multi-disciplinary open access archive for the deposit and dissemination of scientific research documents, whether they are published or not. The documents may come from teaching and research institutions in France or abroad, or from public or private research centers.

L'archive ouverte pluridisciplinaire **HAL**, est destinée au dépôt et à la diffusion de documents scientifiques de niveau recherche, publiés ou non, émanant des établissements d'enseignement et de recherche français ou étrangers, des laboratoires publics ou privés.



Unexpected role of metal halides in a chalcogenide glass network

Rayan Zaiter^a, Mohammad Kassem^a, Daniele Fontanari^a, Anton Sokolov^a, Takeshi Usuki^b, Maria Bokova^a, Alex C. Hannon^c, Chris J. Benmore^d, Fabrice Cousin^e, Ilya Ozheredov^f, Eugene Bychkov^{a,*}

^a Université du Littoral Côte d'Opale, 59140 Dunkerque, France

^b Faculty of Science, Yamagata University, Yamagata 990-8560, Japan

^c ISIS Facility, Rutherford Appleton Laboratory, Chilton, Didcot OX11 0QX, UK

^d X-ray Science Division, Advanced Photon Source, Argonne National Laboratory, Argonne, IL 60439, United States

^e Laboratoire Léon Brillouin, 91191 Gif sur Yvette, France

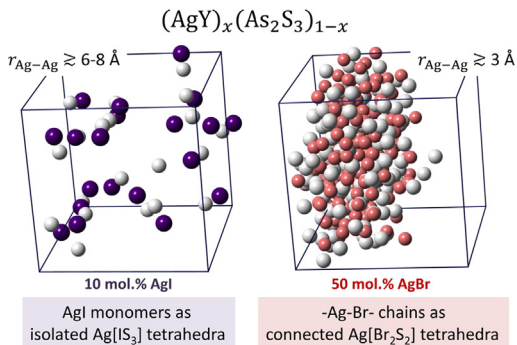
^f Lomonosov Moscow State University, 119991 Moscow, Russian Federation



HIGHLIGHTS

- Silver halides in AgY-As₂S₃ (Y = Br, I) glasses behave as unconventional modifiers.
- Formation of terminal sulfur with AgY additions is accompanied by increasing fraction of As-As homopolar bonds for 16% of arsenic species.
- AgY monomers are distributed randomly in AgY-poor glasses ($\lesssim 2\text{-}3$ at.% Ag)
- Edge- and corner-sharing Ag[Br₂S₂] tetrahedra are forming preferential conduction pathways in AgBr-rich glasses ($\gtrsim 10$ at.% Ag)

GRAPHICAL ABSTRACT



ARTICLE INFO

Article history:

Received 15 December 2021

Revised 10 March 2022

Accepted 11 March 2022

Available online 15 March 2022

Keywords:

Silver halide glasses
Mixed silver and arsenic environment
Neutron and X-ray diffraction
Raman spectroscopy
Small-angle neutron scattering
FPMD modeling

ABSTRACT

Chalcogenide glasses containing light alkali and Group 11 (Cu, Ag) halides MY (Y = Cl, Br, I) exhibit high ionic conductivity while their heavy alkali counterparts show promising properties for optical applications. The structural role of metal halides in chalcogenide glass networks remains either essentially unknown (alkali halides) or controversial (CuY, AgY). In addition, possible structural changes as a function of MY content have not been reported. Using pulsed neutron diffraction, high-energy X-ray scattering, Raman spectroscopy and FPMD modeling, we show unexpected role of silver halides as unconventional modifiers taking two contrasting glass compositions: $(\text{AgI})_{0.1}(\text{As}_2\text{S}_3)_{0.9}$ (critical percolation domain) and $(\text{AgBr})_{0.5}(\text{As}_2\text{S}_3)_{0.5}$ (modifier-controlled region) as an example. The latter alloy seems to be a promising precursor for thermoelectric applications. The deep insight into the glass structure on the short- and intermediate-range scale, including an enhanced chemical disorder, enables a rational design of these functional materials.

© 2022 The Author(s). Published by Elsevier Ltd. This is an open access article under the CC BY-NC-ND license (<http://creativecommons.org/licenses/by-nc-nd/4.0/>).

1. Introduction

Chalcogenide glasses containing alkali and Group 11 (Cu, Ag) halides MY (Y = Cl, Br, I) are promising materials for various appli-

* Corresponding author.

E-mail address: bychkov@univ-littoral.fr (E. Bychkov).

cations. The light alkali and AgY/CuY vitreous chalcogenide alloys exhibit high ionic conductivity [1–4] while their heavy alkali counterparts show excellent optical properties, see for example, [5,6] and references therein. The structural role of metal halides in chalcogenide glass networks remains either essentially unknown (alkali halides) or controversial (CuY, AgY). In addition, possible structural changes as a function of MY content have not been reported. A common point of view related to silver halide glasses consists in considering AgY additions as *chemically inert* dopant salts providing network expansion and additional free volume for fast ion transport associated with a large size of the halide anion [7]. A widely discussed problem was related to anion distribution in glasses with two contrasting hypotheses: (a) clustering of silver halide rich domains of $\alpha\text{-AgI}$ type or (b) a statistical distribution within disordered network [8]. Comparing three silver halides, AgCl, AgBr and AgI, and the resulting glass-forming ability, we have observed that silver bromide and iodide behave more or less similarly, and the glass-forming limits are nearly identical with a slight improvement for AgI. AgCl-As₂X₃ (X = S, Se) and AgCl-Sb₂S₃ glasses are less stable and the limiting AgCl concentration is lower compared to bromide and iodide counterparts. It looks like chloride species are destabilizing the glass network but this observation will need additional studies.

The network expansion with a cubic scaling relation between the conductivity enhancement and the resulting free volume, $\sigma(x)/\sigma(0) \propto [(V_m(x) - V_m(0)/V_m(x)]^3$, where $\sigma(x)$ and $V_m(x)$ are the conductivity and molar volume of the doped glass with a AgY molar fraction x, cannot be applied to AgY-containing chalcogenide glasses [9]. In case of pseudo-binary (AgY)_x(As₂X₃)_{1-x} vitreous alloys, where X = S, Se, or Te, alloying with AgY even decreases the molar volume $V_m(x)$ with increasing x for X = Cl and Br, or $V_m(x)$ remains invariant for AgI-As₂S₃ glasses [10]. Nevertheless, the ionic conductivity $\sigma_i(y)$ of the AgY – As₂S₃ glasses increases by 13 orders of magnitude over 5 orders of magnitude in the silver content y [10], confirming two drastically different ion transport regimes in silver halide thioarsenate glasses, Fig. 1.

The ionic conductivity in the critical percolation domain, $20 \text{ ppm} < y \leq 2 \text{ at.\% Ag}$, follows a power-law dependence, $\sigma_i(y, T) \propto y^{T_0/T}$, where the critical temperature T_0 is related to the connectivity of the glassy host and the average coordination number $\langle n_0 \rangle$ [2]. Moreover, Fig. 1 shows that $\sigma_i(y, T)$ is chemically invariant in the critical percolation domain. Three silver thioarsenate glass families, AgY- and Ag₂S-As₂S₃, reveal identical ionic conductivity within experimental uncertainty over three orders of magnitude in the silver content y. The ionic conductivity in the percolation domain should be sensitive to the stoichiometry of the host glassy matrix, affecting the average coordination number $\langle n_0 \rangle$ [2]. However, slight deviations in the As content will not change significantly $\langle n_0 \rangle$ and therefore $\sigma_i(y, T)$. The ionic conductivity diverges in the modifier-controlled region, $y > 7\text{--}10 \text{ at.\% Ag}$, and the difference in $\sigma_i(y)$ between AgI- and Ag₂S-As₂S₃ glasses approaches 4 orders of magnitude. The critical percolation and modifier-controlled regimes of the ion transport in glasses are related to random vs. non-random distribution of mobile cations in the glass network, confirmed by small-angle neutron scattering, neutron and high-energy X-ray diffraction [2,15,16] and recent first-principles molecular dynamics (FPMD) modeling for silver thioarsenate and thiogermanate glasses [4].

The main goal of the present contribution is to unravel a previously unknown structural role of silver halides in pseudo-binary AgY-As₂S₃ glasses belonging to the critical percolation domain, (AgI)_{0.1}(As₂S₃)_{0.9} (y = 2.13 at.\% Ag), and modifier-controlled region, (AgBr)_{0.5}(As₂S₃)_{0.5} (y = 14.29 at.\% Ag), using Raman spectroscopy, diffraction techniques and FPMD. The latter alloy also seems to be a promising precursor for thermoelectric applications [17–19], starting from the first patent to recently calculated super-high thermoelectric figure of merit $ZT \approx 7$ for similar metal halides and chalcogenides. A deep insight into the structure will be crucial for improving design of new thermoelectric amorphous materials, including printed thermoelectric sheets [20], as well as phase-change memories [21,22], materials for energy storage [23,24], photodetection [25] and spintronics [26].

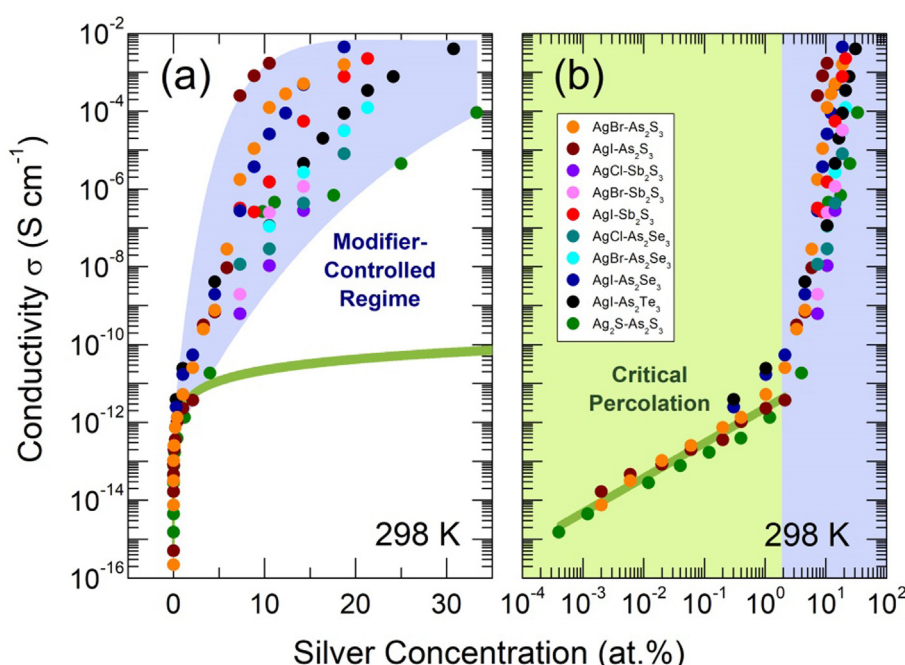


Fig. 1. Room-temperature ionic conductivity isotherms of AgY-As₂S₃ (Y = Br, I), AgY-As₂X₃ (Y = Cl, Br, I; X = Se, Te), AgY-Sb₂S₃ (Y = Cl, Br, I), and Ag₂S-As₂S₃ glasses [10–14]; (a) linear concentration scale, (b) a log-log plot. The bold green solid line shows chemically-invariant power-law composition dependence of $\sigma_{298}(y)$ for three families of silver thioarsenate glasses in the critical percolation domain. The modifier-controlled region is highlighted in light blue. (For interpretation of the references to colour in this figure legend, the reader is referred to the web version of this article.)

2. Methods

2.1. Glass synthesis

The $(\text{AgBr})_{0.5}(\text{As}_2\text{S}_3)_{0.5}$ and $(\text{AgI})_{0.1}(\text{As}_2\text{S}_3)_{0.9}$ glasses were prepared from silver bromide and silver iodide respectively, with arsenic sulfide precursors via conventional high-temperature synthesis. The various components in the required proportion were sealed under vacuum (10^{-6} mbar) in silica tubes, heated up to 850°C for 24 h before quenching in icy salt water.

2.2. Glass homogeneity characterization

A JEOL JSM-7100F thermal field emission scanning electron microscope equipped with EDX Bruker QUANTAX 800 spectrometers was used to check the sample uniformity. The PAXY small-angle neutron scattering instrument (Laboratoire Léon Brillouin, France) was used for mesoscopic ($10\text{--}1000\text{ \AA}$) structural studies using different neutron wavelengths and sample-to-detector distances: $5\text{ \AA}/1.5\text{ m}$, $5\text{ \AA}/3.5\text{ m}$, $8.5\text{ \AA}/5\text{ m}$, and $15\text{ \AA}/6.7\text{ m}$. The velocity selector of the PAXY instrument yielded $\Delta\lambda/\lambda = 0.11$ for the used wavelengths.

2.3. Raman spectroscopy measurements

Raman spectra were collected at room temperature using a Lab-Ram HR spectrometer (Jobin Yvon Horiba Group); in most cases a long working distance microscope objective ($50\times$, 0.50NA) was applied. Raman scattering was excited by a 785 nm solid-state laser and recorded in the $80\text{--}850\text{ cm}^{-1}$ spectral range. To avoid crystallization of the glassy samples, the laser power was chosen between $150\text{ }\mu\text{W}$ and 1.5 mW , and the acquisition time was 100 to 300 s. Two to three spectra were registered for each sample at different positions to verify the sample homogeneity and the absence of photo-induced phenomena. At least, two samples of each composition were studied to check the reproducibility of the data. Some characteristic Raman spectra showing the effect of the laser power and glass reproducibility are given in [Supplementary material](#), Figures S1 and S2.

2.4. Diffraction measurements

The $\text{AgY-As}_2\text{S}_3$ glasses were measured using time-of-flight neutron diffraction at the ISIS spallation neutron source (Rutherford-Appleton Laboratory, UK). The GEM diffractometer at ISIS provides diffraction data over an extended range in reciprocal space up to 50 \AA^{-1} , leading to a high resolution in real space. The neutron diffraction data were corrected for background and container scattering, self-attenuation, multiple scattering, and inelasticity (Placzek) effects to obtain the total neutron structure factor $S_N(Q)$ [27].

High-energy X-ray diffraction measurements were conducted at the 6-ID-D beamline of the Advanced Photon Source (Argonne National Laboratory, USA). The X-ray energy was 100 keV, providing data at Q values up to 30 \AA^{-1} . A 2D setup was used for data collection with a Perkin Elmer model 1621 X-ray area detector. The two-dimensional diffraction patterns were reduced using the Fit2D software [28]. The measured background intensity was subtracted, and corrections were made for the different detector geometries and efficiencies, sample self-attenuation, and Compton-scattering using standard procedures [29] giving the X-ray total structure factor $S_X(Q)$.

2.5. First-principles molecular dynamics modeling

The Born-Oppenheimer molecular dynamics calculations were performed with the CP2K package [30] using the generalized gradi-

ent approximation and the PBEsol exchange–correlation functional [31]. Basically, the employed FPMD technique was similar to that used in previously published reports on similar glass systems [32–34]. Randomly generated initial configurations of 940 atoms, $(\text{AgI})_{0.1}(\text{As}_2\text{S}_3)_{0.9}$, and 1050 atoms, $(\text{AgBr})_{0.5}(\text{As}_2\text{S}_3)_{0.5}$, were optimized using RMC++ code [35] to obtain a good agreement with neutron and high-energy X-ray diffraction results. The cubic box sizes were chosen to match the experimental number density. Further optimization was carried out using DFT with the consecutive basis sets SZV, DZVP and TZVP. We should note that in the RMC optimization we only used coordination number constraints since the DFT optimization at 0 K decreases the total energy of the system substantially, also changing the electronic structure.

The FPMD simulations included sample annealing above the glass transition temperature, 56 ps at 500 K for $(\text{AgI})_{0.1}(\text{As}_2\text{S}_3)_{0.9}$ and 32 ps at 450 K for $(\text{AgBr})_{0.5}(\text{As}_2\text{S}_3)_{0.5}$, using a Nosé-Hoover thermostat chain controlling the temperature [36,37] and the final modeling over 50 ps or 38 ps at 300 K for the two systems, respectively. Further FPMD details can be found in [Supplementary material](#), including Figures S3 and S4, and elsewhere [38–40].

3. Results and discussions

3.1. Glass homogeneity

Similarly to $\text{Ag}_2\text{S-As}_2\text{S}_3$ glasses [14,16,41,42], the $(\text{AgY})_x(\text{As}_2\text{S}_3)_{1-x}$ vitreous alloys are homogeneous at low silver content, $x \lesssim 0.1\text{--}0.2$ (2–4 at.% Ag), and phase-separated above this limit [10]. However, in contrast to homogeneous silver-rich thioarsenate glasses at $y \gtrsim 20$ at.% Ag, the AgY-rich thioarsenate compositions do not reach the second homogeneous glass domain and remain phase-separated at the limit of the glass-forming range, $y_{max} = 14.3$ at.% Ag ($x = 0.5$).

The small-angle neutron scattering (SANS) data for glassy $\text{g-As}_2\text{S}_3$, $(\text{AgBr})_{0.1}(\text{As}_2\text{S}_3)_{0.9}$ and $(\text{AgBr})_{0.5}(\text{As}_2\text{S}_3)_{0.5}$ are shown in Fig. 2(a). The corrected and normalized SANS intensity $I(Q)$ is very similar for homogeneous $\text{g-As}_2\text{S}_3$ and $(\text{AgBr})_{0.1}(\text{As}_2\text{S}_3)_{0.9}$ alloys. These homogeneous chalcogenide glasses exhibit weak small-angle signal, $I(Q) \approx 10^{-4}\text{ cm}^{-1}$ at $Q \approx 0.05\text{ \AA}^{-1}$, related to density fluctuations, which are often described by the Debye-Bueche (DB) model [43], the solid line in Fig. 2(a), see [Supplementary material](#) for further details. Similar $I(Q)$'s were reported for different homogeneous chalcogenide glasses [16,44,45], and the density fluctuations reveal a characteristic DB length scale $\xi \approx 200\text{ \AA}$.

The phase-separated $(\text{AgBr})_{0.5}(\text{As}_2\text{S}_3)_{0.5}$ glass, Fig. 2(b), exhibits by a factor of 100 higher SANS intensity $I(Q)$ below $Q < 0.1\text{ \AA}^{-1}$, roughly following the Porod law, $I(Q) \propto Q^{-4}$ [46]. Nevertheless, the exact shape of $I(Q)$ is more complicated with positive and negative deviations from the Porod slope $n = \partial \log I(Q)/\partial \log Q = -4$. The accessible Q -range ($Q_{min} \approx 2 \times 10^{-3}\text{ \AA}^{-1}$) does not enable following further evolution, most probably a Guinier regime [46], $n = -2$, at lower Q . The Kratky plot, $Q^2 I(Q)$ vs. Q , Fig. 2(c), is often used to estimate a typical size of mesoscopic particles if the Guinier approximation is valid [46,47]. In this case, the function $Q^2 I(Q)$ plotted versus the scattering vector Q shows a maximum. The position of this maximum, Q_{max} , and the Guinier radius of gyration R_g are related, $Q_{max} = \sqrt{3}/R_g$. Here again, the limited Q -range does not allow to observe a clear maximum. Nevertheless, a rough estimation of $R_g = 800 \pm 200\text{ \AA}$ is consistent with the smallest particles observed by SEM, the upper right corner of Fig. 2(b).

3.2. Raman spectra

Typical Raman spectra of the $\text{AgY-As}_2\text{S}_3$ glasses and related references are shown in Figs. 3 and 4. The spectral shape of $(\text{AgI})_{0.1}(\text{As}_2\text{S}_3)_{0.9}$

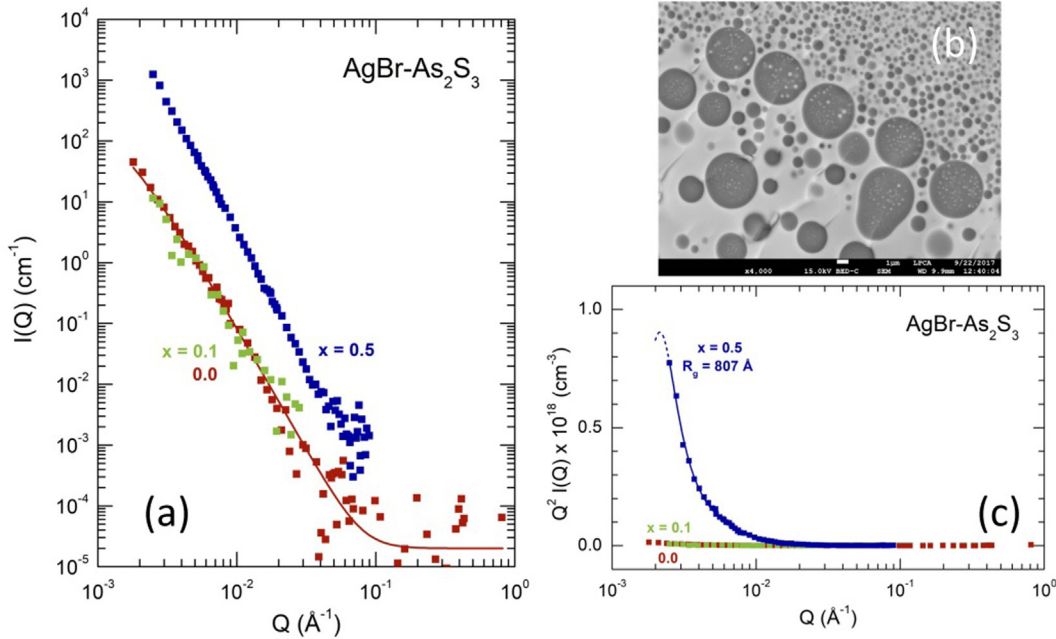


Fig. 2. Homogeneity of $(\text{AgBr})_x(\text{As}_2\text{S}_3)_{1-x}$ glasses, where $x = 0, 0.1$ and 0.5 : (a) corrected and normalized small-angle scattering function $I(Q)$; (b) a SEM image of glassy $(\text{AgBr})_{0.5}(\text{As}_2\text{S}_3)_{0.5}$; (c) the Kratky plots, $Q^2 I(Q)$ vs. Q , for $\text{AgBr}-\text{As}_2\text{S}_3$ glasses. The solid brown line in (a) represents a Debye-Bueche fit for g-As₂S₃ with a typical size of DB density fluctuations $\xi \approx 200$ Å. The solid blue line in (c) shows estimation of the Guinier radius of gyration R_g using a Voigt function. (For interpretation of the references to colour in this figure legend, the reader is referred to the web version of this article.)

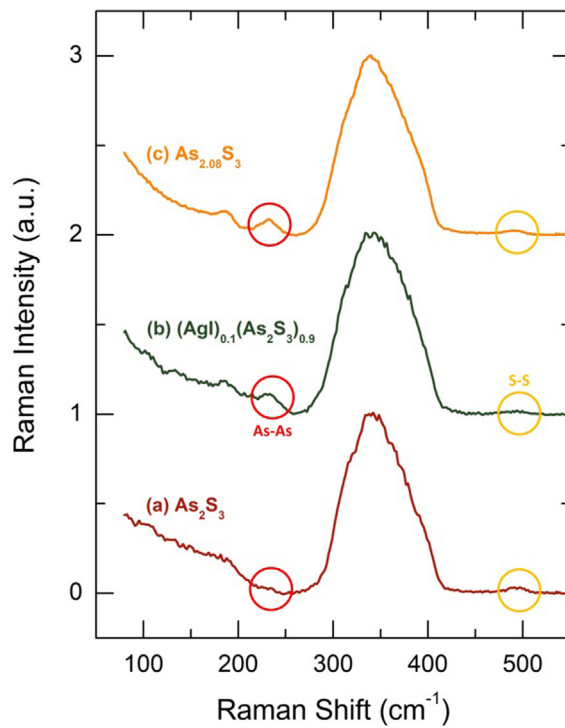


Fig. 3. Raman spectra of glassy (a) As_2S_3 , (b) $(\text{Agl})_{0.1}(\text{As}_2\text{S}_3)_{0.9}$ and (c) As-enriched $\text{As}_{2.08}\text{S}_3 = \text{As}_{0.41}\text{S}_{0.59}$. The As-As stretching at 230 cm^{-1} and S-S stretching at 490 cm^{-1} are emphasized by red and yellow circles, respectively. See corresponding text for further details. (For interpretation of the references to colour in this figure legend, the reader is referred to the web version of this article.)

As_2S_3 _{0.9} is mostly similar to that in glassy As_2S_3 . A broad unresolved feature, centered at $\approx 340 \text{ cm}^{-1}$ and corresponding symmetric and asymmetric As-S stretching [48–50], appears essentially intact while both high-frequency ($\approx 490 \text{ cm}^{-1}$) and low-frequency ($\omega < 250 \text{ cm}^{-1}$) modes exhibit characteristic changes.

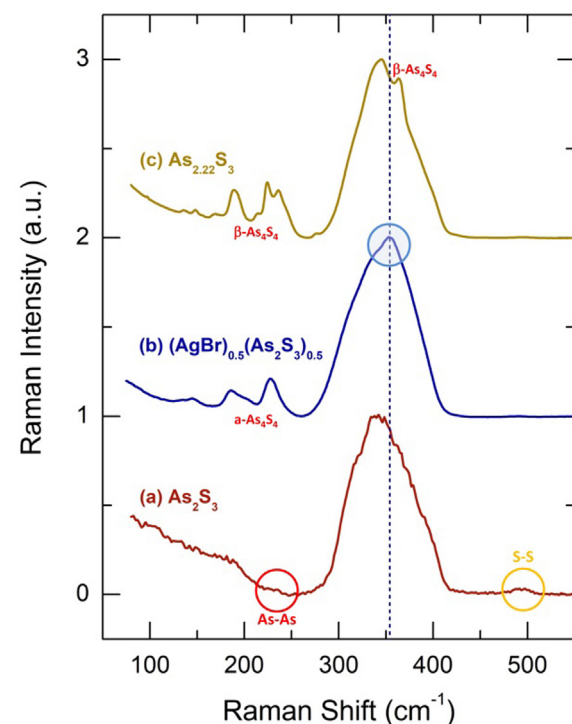


Fig. 4. Raman spectra of glassy (a) As_2S_3 , (b) $(\text{AgBr})_{0.5}(\text{As}_2\text{S}_3)_{0.5}$, (c) glassy-crystalline $\text{As}_{2.22}\text{S}_3 \cong \text{As}_{0.43}\text{S}_{0.57}$. Raman features of β -As₄S₄ and a-As₄S₄ can be identified for $\text{As}_{2.22}\text{S}_3$ and $(\text{AgBr})_{0.5}(\text{As}_2\text{S}_3)_{0.5}$, respectively, in addition to a distinct feature at 354 cm^{-1} for glassy $(\text{AgBr})_{0.5}(\text{As}_2\text{S}_3)_{0.5}$, blue circle. (For interpretation of the references to colour in this figure legend, the reader is referred to the web version of this article.)

The two features are related to chemical disorder in stoichiometric g-As₂S₃ [45,51–54], corresponding to S-S and As-As stretching, respectively. Adding silver iodide, one observes a decrease of S-S dimers with a corresponding increase of As-As homopolar

bonds, similar to that in As-enriched nearly stoichiometric glassy $\text{As}_{2.08}\text{S}_3$, Fig. 3(c). The observed increase in intensity of the 230 cm^{-1} peak, emphasized by a red circle in Fig. 3, is accompanied by a second low-frequency feature at $\approx 180\text{ cm}^{-1}$, probably indicating the appearance of As_4S_4 monomeric cages in the glass network [51,54]. The increasing population of As-As bonds is amplified on further silver halide additions, Fig. 4. Glassy $(\text{AgBr})_{0.5}(\text{As}_2\text{S}_3)_{0.5}$ shows a distinct signature of amorphous As_4S_4 [55] in contrast to nanocrystallites of high- T realgar polymorph $\beta\text{-As}_4\text{S}_4$ [51] in glassy/crystalline $\text{As}_{2.22}\text{S}_3$.

The AgBr -rich glass also shows a new spectroscopic feature at 354 cm^{-1} emphasized by a blue circle in Fig. 4(b) and absent in g- As_2S_3 and As-rich sulfide glasses. This emerging peak appears to be similar to that reported earlier for Ag_2S - As_2S_3 glasses with increasing silver sulfide content. Fig. 5 shows the Raman spectra of $(\text{AgBr})_{0.5}(\text{As}_2\text{S}_3)_{0.5}$ and $(\text{Ag}_2\text{S})_{0.35}(\text{As}_2\text{S}_3)_{0.65}$ glasses in comparison with crystalline silver thioarsenate compounds AgAsS_2 and Ag_3AsS_3 . In addition, a scaled spectroscopic envelope for g- As_2S_3 was subtracted from the spectra of glasses revealing changes in the spectra with increasing AgBr or Ag_2S content.

The vitreous $(\text{Ag}_2\text{S})_{0.35}(\text{As}_2\text{S}_3)_{0.65}$ composition is on the border between phase-separated and homogeneous glasses in the Ag_2S - As_2S_3 system [42] and exhibits the Raman spectrum which is similar to those published previously [57,58]. In addition, the silver content in the two thioarsenate glasses is comparable: 14.3 at.% for $(\text{AgBr})_{0.5}(\text{As}_2\text{S}_3)_{0.5}$ and 16.3 at.% for $(\text{Ag}_2\text{S})_{0.35}(\text{As}_2\text{S}_3)_{0.65}$. Fig. 5 reveals that both the entire and difference Raman spectra of these glasses are rather similar. Moreover, the difference spectra are reminiscent of the Raman spectra for crystalline AgAsS_2 and Ag_3AsS_3 polymorphs: smithite [56] and trechmannite (this work),

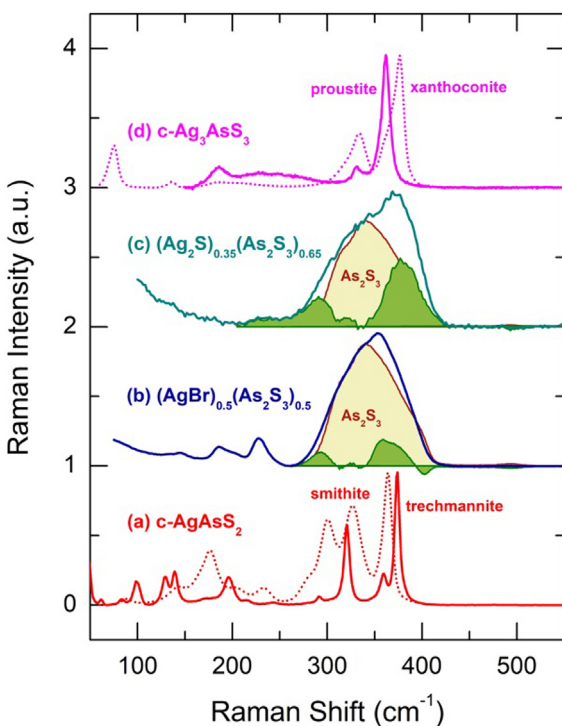


Fig. 5. Raman spectra of silver-containing glasses and Ag_2S - As_2S_3 crystalline references: (a) AgAsS_2 crystals, the solid red line corresponds to trechmannite (this work), the dotted red line to smithite [56]; (b) $(\text{AgBr})_{0.5}(\text{As}_2\text{S}_3)_{0.5}$ glass; (c) $(\text{Ag}_2\text{S})_{0.35}(\text{As}_2\text{S}_3)_{0.65}$ glass; (d) Ag_3AsS_3 crystals, the solid magenta line corresponds to proustite (this work), the dotted magenta line to xanthoconite [56]. The scaled spectroscopic envelope of vitreous As_2S_3 used for glass subtraction is highlighted in light yellow; the silver-related difference spectrum is highlighted in green. See text for further details. (For interpretation of the references to colour in this figure legend, the reader is referred to the web version of this article.)

proustite (this work) and xanthoconite [56], respectively. Consequently, the broad high-frequency feature, $350\text{ cm}^{-1} \lesssim \omega \lesssim 400\text{ cm}^{-1}$, seems to be related to As-S stretching in either As_3S_3 rings, present in the crystalline structure of AgAsS_2 [59,60], or isolated AsS_3 pyramidal units, characteristic of the Ag_3AsS_3 lattice [61,62].

3.3. Neutron and X-ray diffraction data

Weighted average structure factors $S(Q)$ were derived from the measured scattering cross section per atom $d\sigma/d\Omega$ through the relation:

$$\frac{d\sigma}{d\Omega} = \left| \sum_{\alpha} c_{\alpha} \bar{b}_{\alpha} \right|^2 [S(Q) - 1] + \sum_{\alpha} c_{\alpha} \bar{b}_{\alpha}^2 \quad (1)$$

in the case of neutron scattering, where c_{α} , \bar{b}_{α} , and \bar{b}_{α}^2 are, respectively, the atomic concentration, the average of the neutron-nucleus scattering length, and the mean square scattering length of element α . In the X-ray case, \bar{b}_{α} in Eq. (1) is replaced by $f_{\alpha}(Q)$, the atomic scattering factor of element α , which is Q -dependent.

The average structure factor $S(Q)$ of a polyatomic system can be decomposed into Faber-Ziman partial structure factors $S_{\alpha\beta}(Q)$ for (α, β) -atomic pairs.

$$S(Q) = \sum_{\alpha, \beta} w_{\alpha\beta} S_{\alpha\beta}(Q) \quad (2)$$

and the neutron weighting factors are defined as

$$w_{\alpha\beta}^N = (2 - \delta_{\alpha\beta}) \frac{c_{\alpha} \bar{b}_{\alpha} c_{\beta} \bar{b}_{\beta}}{\left| \sum_{\alpha} c_{\alpha} \bar{b}_{\alpha} \right|^2} \quad (3)$$

where $\delta_{\alpha\beta}$ is the Kronecker delta function. Likewise, in the X-ray case, the average neutron coherent scattering lengths are replaced by Q -dependent atomic scattering factors.

Typical neutron $S_N(Q)$ and X-ray $S_X(Q)$ structure factors for the AgY - As_2S_3 glasses and g- As_2S_3 are shown in Figs. 6 and 7, respectively. The AgI -poor glass reveals similar diffraction pattern to vitreous arsenic sulfide with distinct first sharp diffraction peak (FSDP) at $Q_0 \approx 1.2\text{ \AA}^{-1}$ and the most intense second principal peak (PP2) at $Q_2 \approx 3.9\text{ \AA}^{-1}$. In contrast, both $S_N(Q)$ and $S_X(Q)$ for silver-rich glassy $(\text{AgBr})_{0.5}(\text{As}_2\text{S}_3)_{0.5}$ show a strongly reduced FSDP, the most intense principal peak (PP) at $Q_1 \approx 2.3\text{ \AA}^{-1}$, and some indications of the enhanced small-angle scattering below 0.5 \AA^{-1} . Similar trends were observed earlier for Ag_2S - As_2S_3 glasses [15], except small-angle scattering at low Q for silver-rich glasses, and indicate significant changes in intermediate-range ordering as well as the network contraction with increasing Ag_2S or AgY content.

To extract the parameters of the FSDP, a Voigt function was used to approximate the background underneath it, allowing the FSDP to be isolated and fitted, see Figure S5 in Supplementary material and related references. The isolated FSDPs are shown in Fig. 8, and the fitting parameters are collected in Table 1. The FSDP position Q_0 remains essentially invariant both in neutron and X-ray data, $Q_0 = 1.23 \pm 0.03\text{ \AA}^{-1}$, while the FSDP area A_0 is smaller for X-rays. The last trend is simply related to different As-As neutron and X-ray weightings, $w_{\text{As}-\text{As}}^N$ and $w_{\text{As}-\text{As}}^X(Q)$, since the FSDP mostly reflects periodicity of the glass-forming species at the intermediate-range scale confirmed by neutron diffraction with isotopic substitution [63] and anomalous X-ray scattering [64]. Table 1 shows that the weighted FSDP areas are comparable, $A_0^N/w_{\text{As}-\text{As}}^N \cong A_0^X/w_{\text{As}-\text{As}}^X(Q)$, and confirms changes in the intermediate range ordering for vitreous $(\text{AgBr})_{0.5}(\text{As}_2\text{S}_3)_{0.5}$ compared to $(\text{AgI})_{0.1}(\text{As}_2\text{S}_3)_{0.9}$ and As_2S_3 glasses.

The neutron $T_N(r)$ and X-ray $T_X(r)$ total correlation functions were derived through the usual Fourier transform,

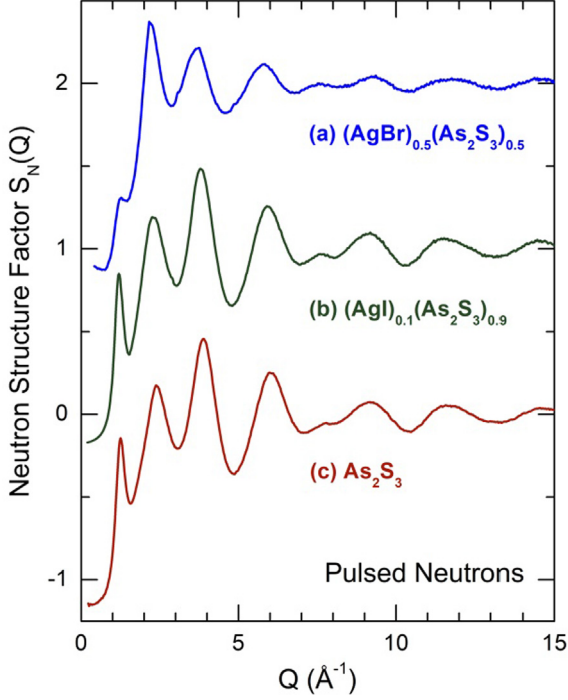


Fig. 6. Neutron structure factors $S_N(Q)$ of (a) $(\text{AgBr})_{0.5}(\text{As}_2\text{S}_3)_{0.5}$, (b) $(\text{AgI})_{0.1}(\text{As}_2\text{S}_3)_{0.9}$, and (c) As_2S_3 glasses over a limited Q -range.

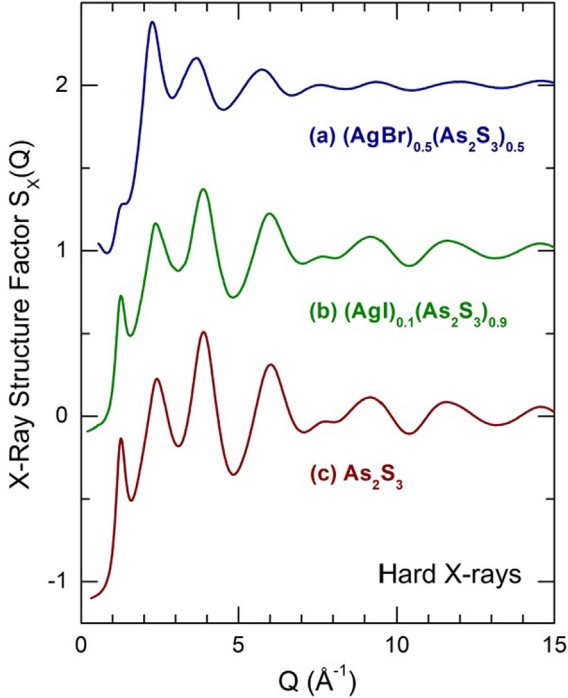


Fig. 7. X-ray structure factors $S_X(Q)$ of (a) $(\text{AgBr})_{0.5}(\text{As}_2\text{S}_3)_{0.5}$, (b) $(\text{AgI})_{0.1}(\text{As}_2\text{S}_3)_{0.9}$, and (c) As_2S_3 glasses over a limited Q -range.

$$T(r) = 4\pi\rho_0 r + \frac{2}{\pi} \int_0^{Q_{\max}} Q[S(Q) - 1] \sin(Qr) M(Q) dQ \quad (4)$$

where ρ_0 is the atomic number density, and $M(Q)$ is the Lorch modification function.

Typical $T_N(r)$ and $T_X(r)$ functions for $(\text{AgY})_x(\text{As}_2\text{S}_3)_{1-x}$ glasses and $g\text{-As}_2\text{S}_3$ are shown in Figs. 9 and 10. Increasing the AgY content,

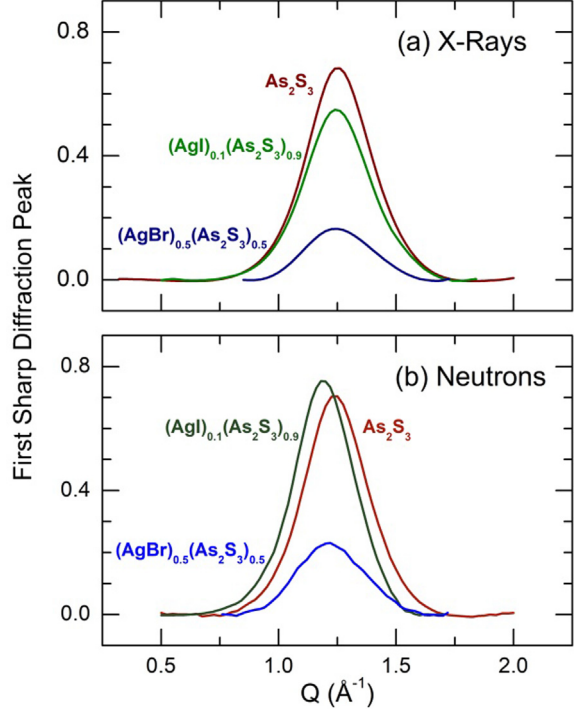


Fig. 8. Isolated FSDPs of $\text{AgY}\text{-As}_2\text{S}_3$ glasses in (a) X-ray and (b) neutron diffraction data.

one observes systematic changes in the real-space functions. The first peak at 2.27\AA , related to As-S first neighbors, decreases, while new high- r features between $2.5 \text{\AA} \leq r \leq 3.0 \text{\AA}$ emerge and grow with x . The second neighbor peak at 3.5\AA broadens and a new feature appears at $\approx 4.1 \text{\AA}$. Finally, more distant correlations at $r > 5 \text{\AA}$ are progressively becoming flat indicating disappearance of the intermediate range order, characteristic of $g\text{-As}_2\text{S}_3$, which is also seen in the FSDP systematics.

A closer look at the $T_N(r)$ and $T_X(r)$ functions for glassy $(\text{AgI})_{0.1}(-\text{As}_2\text{S}_3)_{0.9}$, Fig. 11, reveals multiple contributions within the $2.5 \text{\AA} \leq r \leq 3.0 \text{\AA}$ range. The neutron data shows a distinct feature at 2.6\AA and a shoulder at 2.8\AA , while the $T_X(r)$ exhibits an opposite trend; a clear feature at 2.8\AA with a shoulder at lower interatomic distances.

The 2.8\AA feature corresponds to Ag-I atomic pairs with interatomic distances, $2.75 \text{\AA} \leq r_{\text{Ag}-\text{I}} \leq 2.85 \text{\AA}$, observed in different crystalline and amorphous solids and liquids [11,65,66]. In addition, a significantly higher amplitude of the 2.8\AA peak in the X-ray data correlates with the Ag-I weightings, $w_{\text{Ag}-\text{I}}^N/w_{\text{Ag}-\text{I}}^X(Q) = 0.248$, for glassy $(\text{AgI})_{0.1}(\text{As}_2\text{S}_3)_{0.9}$. However, the maximum possible Ag-I coordination appears to be unrealistically low, $1.0 \leq N_{\text{Ag}-\text{I}} \leq 1.5$, for pure iodine local environment of silver. Typically, silver exhibits a tetrahedral local coordination in crystalline iodides. The 2.6\AA feature cannot, in any circumstances, be related to the Ag-I atomic pairs but a possible alternative, Ag-S first neighbors, seems to be plausible, especially taking into account the Raman spectroscopy results. Typical Ag-S interatomic distances, $2.45 \text{\AA} \leq r_{\text{Ag}-\text{S}} \leq 2.72 \text{\AA}$, in sulfide glasses and crystals [15,32,67] are consistent with this hypothesis. In addition, a new class of metal halide coordination polymers, $\text{MY}-\text{A}_4\text{X}_m$, where $\text{M} = \text{Cu}, \text{Ag}; \text{Y} = \text{Cl}, \text{Br}, \text{I}; \text{A} = \text{P}, \text{As}; \text{X} = \text{S}, \text{Se}; 3 \leq m \leq 4$ [68–70] is characterized by a mixed tetrahedral local environment of the d^{10} cation of different stoichiometry: $1\text{Y} + 3\text{X}$, $2\text{Y} + 2\text{X}$ or $3\text{Y} + 1\text{X}$, depending on the MY content. The mixed silver environment ($1\text{I} + 3\text{S}$) appears to be consistent with the experimental neutron and X-ray results for $(\text{AgI})_{0.1}(\text{As}_2\text{S}_3)_{0.9}$.

Table 1

FSDP parameters for As_2S_3 , $(\text{AgI})_{0.1}(\text{As}_2\text{S}_3)_{0.9}$, and $(\text{AgBr})_{0.5}(\text{As}_2\text{S}_3)_{0.5}$ glasses in neutron and X-ray diffraction data.

AgY	$Q_0^N (\text{\AA}^{-1})$	A_0^N	$A_0^N / w_{\text{As}-\text{As}}^N$	$Q_0^X (\text{\AA}^{-1})$	A_0^X	$A_0^X / w_{\text{As}-\text{As}}^X(Q)$
0	1.24(1)	0.250(5)	0.68(2)	1.26(1)	0.242(5)	0.72(2)
10	1.19(1)	0.246(5)	0.75(2)	1.25(1)	0.198(5)	0.71(3)
50	1.22(1)	0.081(5)	0.55(4)	1.25(1)	0.057(5)	0.50(5)

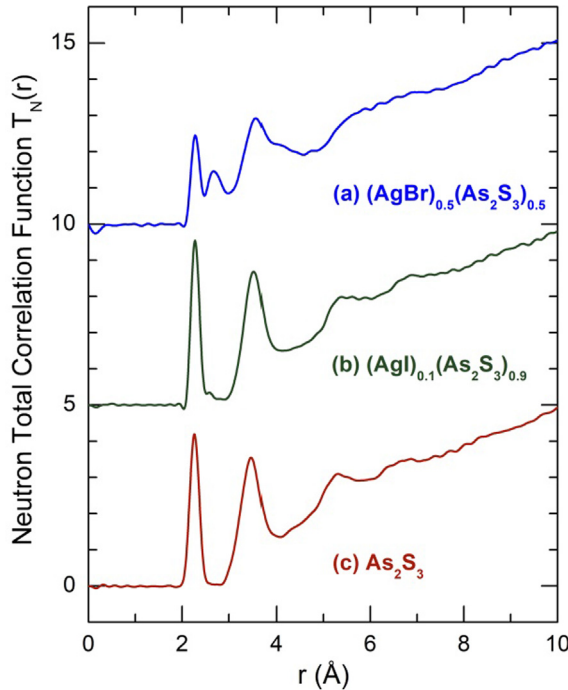


Fig. 9. Neutron total correlation functions for (a) $(\text{AgBr})_{0.5}(\text{As}_2\text{S}_3)_{0.5}$, (b) $(\text{AgI})_{0.1}(\text{As}_2\text{S}_3)_{0.9}$, and (c) As_2S_3 glasses.

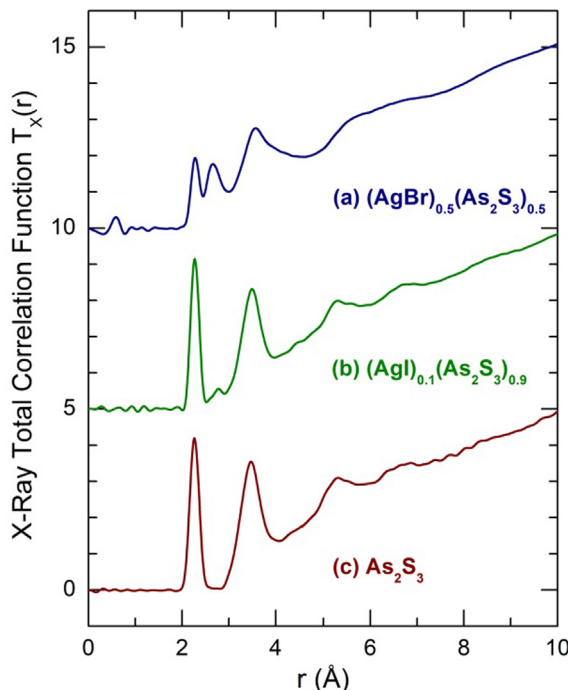


Fig. 10. X-ray total correlation functions for (a) $(\text{AgBr})_{0.5}(\text{As}_2\text{S}_3)_{0.5}$, (b) $(\text{AgI})_{0.1}(\text{As}_2\text{S}_3)_{0.9}$, and (c) As_2S_3 glasses.

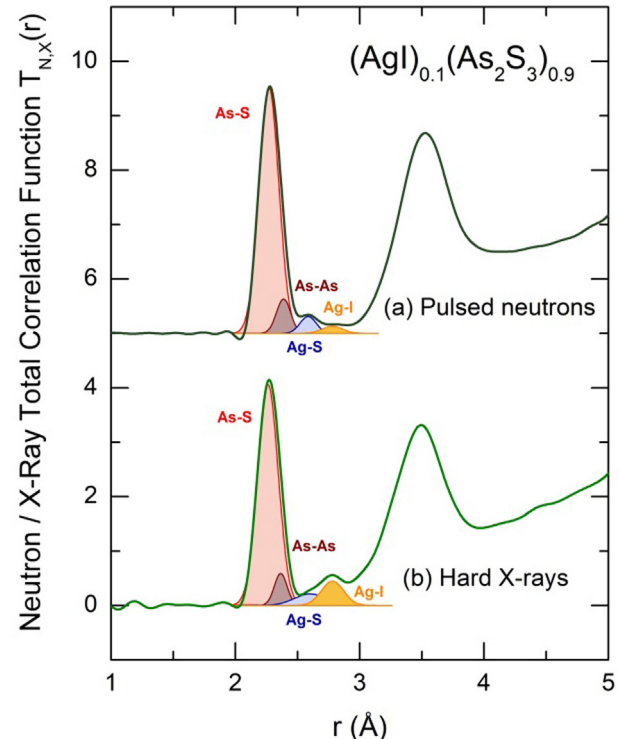


Fig. 11. Fitting the total correlation function for glassy $(\text{AgI})_{0.1}(\text{As}_2\text{S}_3)_{0.9}$: (a) neutron data, (b) X-ray data. The As-S, As-As, Ag-S and Ag-I atomic pairs are highlighted in red, brown, blue and yellow, respectively. (For interpretation of the references to colour in this figure legend, the reader is referred to the web version of this article.)

In our fitting, we constrained the coordination numbers to be equal for ND and XRD but the interatomic distances were left to be free. X-rays and neutrons are scattered differently, by electrons and nuclei, respectively. Consequently, the interatomic distances may vary insignificantly even for monoatomic glass or liquid.

The constrained three-peak fitting (As-S, Ag-S and Ag-I first neighbor contributions) shows, however, arsenic overcoordination, $N_{\text{As}-\text{S}} \approx 3.2$, associated also with a high- r asymmetric broadening of the 2.27 Å peak. Taking into account the increased population of the As-As homopolar bonds, observed in the Raman spectra of the AgY-As₂S₃ glasses, the additional constraint included trigonal arsenic local coordination, $N_{\text{As}-\text{S}} + N_{\text{As}-\text{As}} = 3$, and the forth, As-As, contribution. The corresponding fitting results are shown in Figs. 11 and 12; the derived fitting parameters are collected in Table 2.

The four-peak fitting yields consistent results for both neutron and X-ray data, and reveals the increased population of the As-As first neighbors in glassy $(\text{AgBr})_{0.5}(\text{As}_2\text{S}_3)_{0.5}$, in agreement with the Raman spectroscopy results, Fig. 4. Table 2 shows that the derived As-As first neighbor distances, 2.39 ± 0.04 Å, are reasonably well agreed with interatomic distances in amorphous arsenic and As-rich sulfide glasses [45,71,72]. The derived Ag-Br interatomic separation is also consistent with diffraction results for AgBr-containing glasses, crystals, and liquids, $2.67 \text{ \AA} \leq r_{\text{Ag}-\text{Br}} \leq 2.89 \text{ \AA}$ [73,74]. We should note a different stoichiometry of the mixed sil-

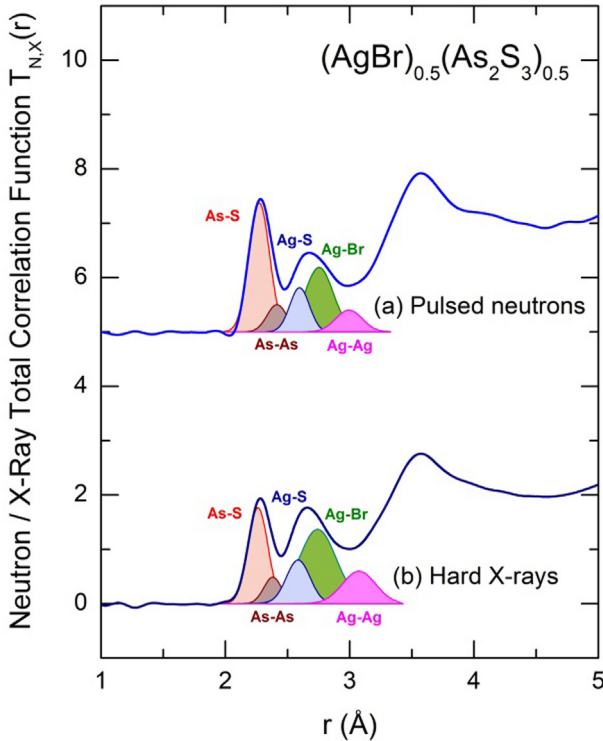


Fig. 12. Fitting the total correlation function for glassy $(\text{AgBr})_{0.5}(\text{As}_2\text{S}_3)_{0.5}$: (a) neutron data, (b) X-ray data. The As-S, As-As, Ag-S, Ag-Br, and Ag-Ag atomic pairs are highlighted in red, brown, blue, green, and magenta, respectively. (For interpretation of the references to colour in this figure legend, the reader is referred to the web version of this article.)

ver local environment in silver-rich $(\text{AgBr})_{0.5}(\text{As}_2\text{S}_3)_{0.5}$, consisting of $2\text{S} + 2\text{Br}$ first neighbors. The derived stoichiometry follows a usual trend in crystalline MY- A_4X_m with increasing MY content. The MY-poor compounds exhibit the $1\text{Y} + 3\text{X}$ stoichiometry while the MY-rich compositions show either 2:2 or 3:1 Y/X ratios [68–70]. Glassy $(\text{AgBr})_{0.5}(\text{As}_2\text{S}_3)_{0.5}$ reveals also rather intense peak at $\approx 3 \text{ \AA}$, which could be related to Ag-Ag short second neighbor contacts, since more intense in the X-ray data. The direct identification and precise coordination of the Ag-Ag second neighbors is hardly possible in a four-component glass without site-sensitive methods as neutron diffraction with isotopic substitution [67,75], anomalous X-ray scattering or low-temperature EXAFS at the Ag K-edge.

3.4. First principles molecular dynamics results

The FPMD simulation boxes for $(\text{AgI})_{0.1}(\text{As}_2\text{S}_3)_{0.9}$ and $(\text{AgBr})_{0.5}(-\text{As}_2\text{S}_3)_{0.5}$ are shown in Figs. 13 and 14. As expected, glassy $(\text{AgI})_{0.1}(-\text{As}_2\text{S}_3)_{0.9}$ appears to be homogeneous with rather random

distribution of Ag-I atomic pairs within the simulation box, Fig. 13(b). Surprisingly, silver-rich $(\text{AgBr})_{0.5}(\text{As}_2\text{S}_3)_{0.5}$ shows a clear separation into AgBr-rich and AgBr-poor phases although the size of the simulation box ($29.62 \times 29.62 \times 29.62 \text{ \AA}^3$) is far below the experimental SANS radius of gyration, $R_g = 800 \pm 200 \text{ \AA}$. The detailed analysis of the FPMD results will be published elsewhere and some additional results are given in [Supplementary material](#). Here we will limit our discussion to three topics related to (i) silver distribution and connectivity in the critical percolation domain, $(\text{AgI})_{0.1}(\text{As}_2\text{S}_3)_{0.9}$, and modifier-controlled region, $(\text{AgBr})_{0.5}(\text{As}_2\text{S}_3)_{0.5}$; (ii) mixed silver and arsenic local environment, and (iii) ring statistics.

The derived FPMD Ag-Ag partial pair-distribution functions $g_{\text{AgAg}}(r)$ for glassy $(\text{AgI})_{0.1}(\text{As}_2\text{S}_3)_{0.9}$ and $(\text{AgBr})_{0.5}(\text{As}_2\text{S}_3)_{0.5}$ are shown in Fig. 15. As expected from Fig. 13(b), the silver-poor glass does not show any direct contact of neighboring AgI units. The shortest Ag-Ag separation distance is centered at $\approx 6 \text{ \AA}$ (16 % of Ag species), and each silver cation has at least one Ag neighbor above $\approx 8 \text{ \AA}$. The phase-separated silver-rich $(\text{AgBr})_{0.5}(\text{As}_2\text{S}_3)_{0.5}$ vitreous alloy exhibits a strongly connected Ag-related subnetwork, clearly visible in Fig. 14. In average, each silver cation has one second neighbor at 3 \AA and additionally three neighboring cations at $\approx 4 \text{ \AA}$, ensuring a heavily correlated Ag^+ ionic motion, characterized by the Haven ratio $H_R \approx 0.4$ [13]. Consequently, the main structural difference between the two ion transport regimes, critical percolation vs. modifier-controlled ionic diffusion, related to random or non-random mobile cation distribution [2], is consistent with the FPMD results.

The FPMD simulated Ag- and As-related partial pair-distribution functions, Figs. 16 and 17, confirm mixed silver and arsenic local environment in both silver-poor $(\text{AgI})_{0.1}(\text{As}_2\text{S}_3)_{0.9}$ and silver-rich $(\text{AgBr})_{0.5}(\text{As}_2\text{S}_3)_{0.5}$. Nevertheless, the simulated partial coordination numbers are slightly different from those found experimentally. The difference is more significant for silver-poor glass.

Each silver cation in $(\text{AgI})_{0.1}(\text{As}_2\text{S}_3)_{0.9}$ has in average three sulfur first neighbors but less than one iodine atom, $N_{\text{Ag}-\text{I}} = 0.47$. In addition, silver also has arsenic nearest neighbors at 2.9 \AA , $N_{\text{Ag}-\text{As}} = 0.28$, thus completing the average total coordination number to nearly tetrahedral local environment, $N_{\text{Ag}-\text{X}} = 3.75$, where X = I, S and As. We note that Ag-As first neighbors were also found in FPMD simulations of glassy AgAsS_2 [32]. The remaining iodine species have moved from silver to arsenic, $N_{\text{I}-\text{As}} = 0.53$, but they are located close to silver at a typical second neighbor distance centered at $\approx 4 \text{ \AA}$. Low silver and iodine atomic concentrations in $(\text{AgI})_{0.1}(\text{As}_2\text{S}_3)_{0.9}$, 2.13 at.%, implies negligible effect on arsenic local environment, $N_{\text{As}-\text{I}} = 0.02$ and $N_{\text{As}-\text{Ag}} = 0.01$. As expected, arsenic has trigonal local coordination with sulfur, $N_{\text{As}-\text{S}} = 2.55$, and arsenic, $N_{\text{As}-\text{As}} = 0.47$, first neighbors, Fig. 17(b). The FPMD simulated fraction of As-As homopolar bonds in $(\text{AgI})_{0.1}(\text{As}_2\text{S}_3)_{0.9}$ exceeds therefore the experimental value by a factor of 2. The enhanced

Table 2

First neighbor interatomic distances r and partial coordination numbers N_{ij} in $(\text{AgI})_{0.1}(\text{As}_2\text{S}_3)_{0.9}$ and $(\text{AgBr})_{0.5}(\text{As}_2\text{S}_3)_{0.5}$ glasses.

As-S		As-As		Ag-S		Ag-Y	
$r (\text{\AA})$	N_{ij}	$r (\text{\AA})$	N_{ij}	$r (\text{\AA})$	N_{ij}	$r (\text{\AA})$	N_{ij}
$(\text{AgI})_{0.1}(\text{As}_2\text{S}_3)_{0.9}$							
ND	2.27(1)	2.76(5)*	2.39(3)	0.24(5)*	2.58(2)	3.00**	2.78(2)
XRD	2.26(1)	2.76(5)*	2.36(3)	0.24(5)*	2.60(2)	3.00**	2.78(2)
$(\text{AgBr})_{0.5}(\text{As}_2\text{S}_3)_{0.5}$							
ND	2.27(1)	2.53(5)*	2.41(3)	0.47(5)*	2.60(2)	2.00**	2.75(2)
XRD	2.26(1)	2.53(5)*	2.38(3)	0.47(5)*	2.59(2)	2.00**	2.74(2)

* Trigonal arsenic local coordination was fixed, $N_{\text{As}-\text{S}} + N_{\text{As}-\text{As}} = 3$, and partial $N_{\text{As}-\text{S}}$ and $N_{\text{As}-\text{As}}$ coordination numbers were constrained to be identical in the neutron and X-ray data fitting.

** Tetrahedral silver local coordination was constrained and fixed, $N_{\text{Ag}-\text{S}} + N_{\text{Ag}-\text{Y}} = 4$, and partial $N_{\text{Ag}-\text{S}}$ and $N_{\text{Ag}-\text{Y}}$ coordination numbers were constrained to be identical in the neutron and X-ray data fitting.

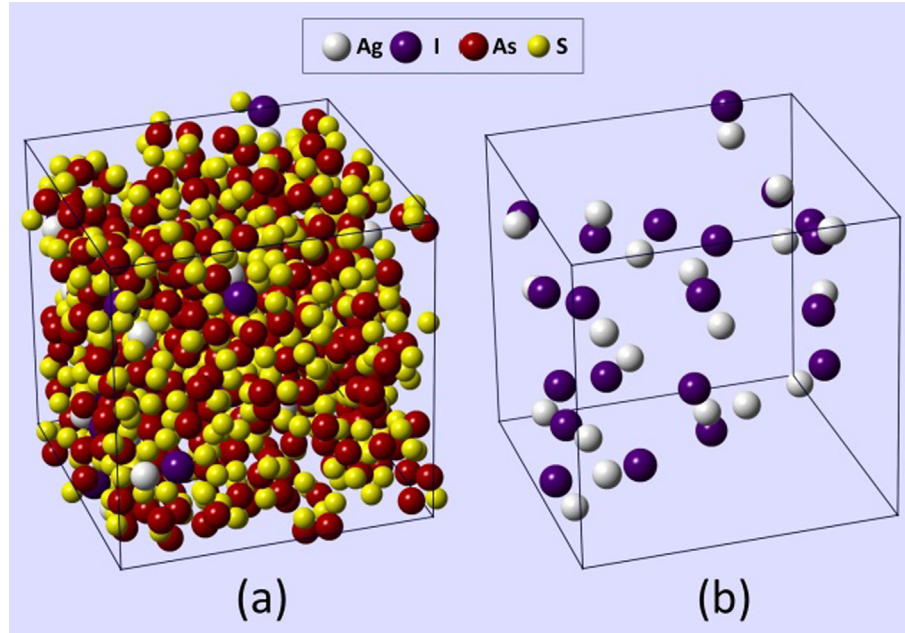


Fig. 13. Typical snapshot of the FPMD simulation box, $(29.014)^3 \text{ \AA}^3$, at 300 K for glassy $(\text{AgI})_{0.1}(\text{As}_2\text{S}_3)_{0.9}$, containing 20 Ag, 20 I, 360 As, and 540 S atomic species: (a) the entire box, (b) only Ag and I species.

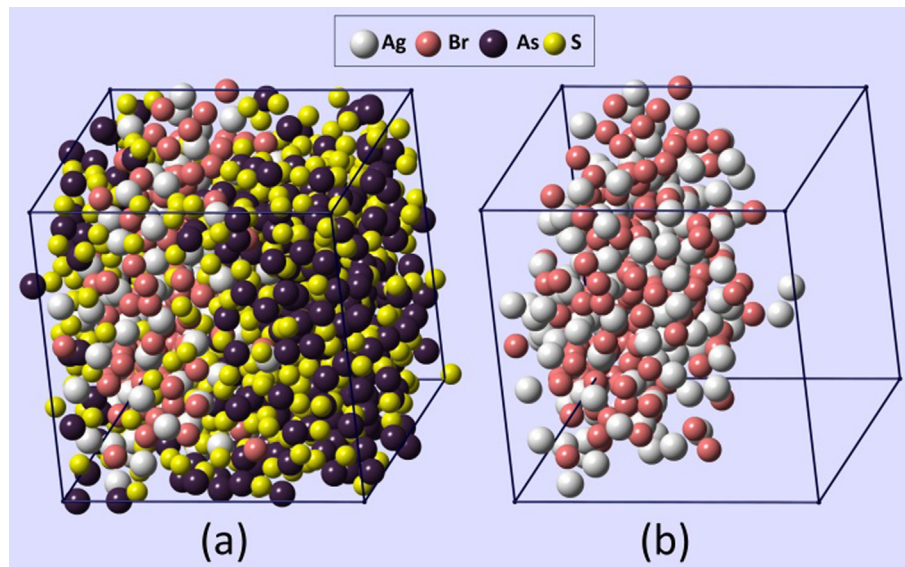


Fig. 14. Typical snapshot of the FPMD simulation box, $(29.62)^3 \text{ \AA}^3$, at 300 K for glassy $(\text{AgBr})_{0.5}(\text{As}_2\text{S}_3)_{0.5}$, containing 150 Ag, 150 Br, 300 As, and 450 S atomic species: (a) the entire box, (b) only Ag and Br species. A clear phase-separation is observed.

chemical disorder in chalcogenide glassy systems seems to be a common feature of FPMD simulations using PBE or PBEsol and requires the use of advanced hybrid functionals, TPSS [76,77], BLYP [78–80] or PBE0 [38–40], to improve the agreement with experiments. Nevertheless, the simulated partial functions reflect reasonably well the diffraction results.

The FPMD simulated silver local environment in $(\text{AgBr})_{0.5}(\text{As}_2\text{S}_3)_{0.5}$ is closer to the derived experimental parameters: $N_{\text{Ag-S}} = 1.73$ and $N_{\text{Ag-Br}} = 2.20$ with negligible contribution from arsenic nearest neighbors, $N_{\text{Ag-As}} = 0.05$, Fig. 16(a). The trigonal arsenic local coordination consists of sulfur, $N_{\text{As-S}} = 2.33$, arsenic, $N_{\text{As-As}} = 0.51$, and bromine, $N_{\text{As-Br}} = 0.13$, first neighbors. The majority of bromine species are connected to silver, 82 %, in con-

trast to $(\text{AgI})_{0.1}(\text{As}_2\text{S}_3)_{0.9}$, where the fraction of I-Ag atomic pairs is just 47 %.

The ring statistics in glassy As_2S_3 , $(\text{AgI})_{0.1}(\text{As}_2\text{S}_3)_{0.9}$ and $(\text{AgBr})_{0.5}(\text{As}_2\text{S}_3)_{0.5}$, calculated using the R.I.N.G.S. code [81], is shown in Fig. 18. The majority of rings in g- As_2S_3 are chemically ordered, As_pS_q , where $p = q$ and $p + q$ is the ring size, since the chemical disorder is small, $[\text{As-As}] / ([\text{As-As}] + [\text{As-S}]) = 0.02\text{--}0.03$. The ring distribution is bimodal with two maxima centered at small, $3 \leq p + q \leq 6$, and big, $14 \leq p + q \leq 36$, rings. We note a significant fraction of edge-sharing ES- As_2S_3 pyramidal units ($p+q=4$), also reported previously in a small-box FPMD simulation of glassy arsenic sulfide [82]. Surprisingly, the fraction of the 12-membered rings is small even though the $p+q=12$ rings are the only elements

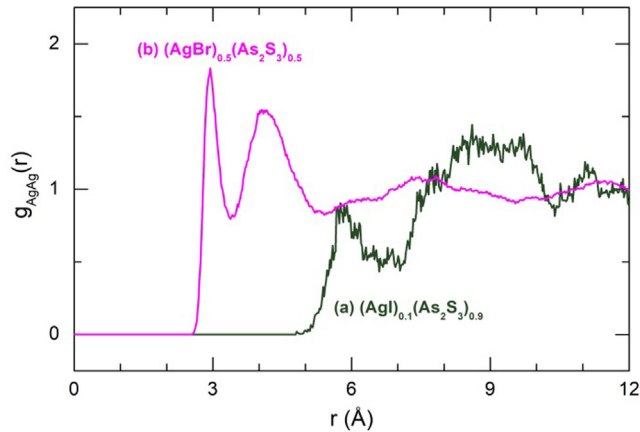


Fig. 15. FPMDF Ag-Ag partial pair-distribution function $g_{\text{AgAg}}(r)$ in (a) $(\text{AgI})_{0.1}(\text{As}_2\text{S}_3)_{0.9}$ and (b) $(\text{AgBr})_{0.5}(\text{As}_2\text{S}_3)_{0.5}$ glasses.

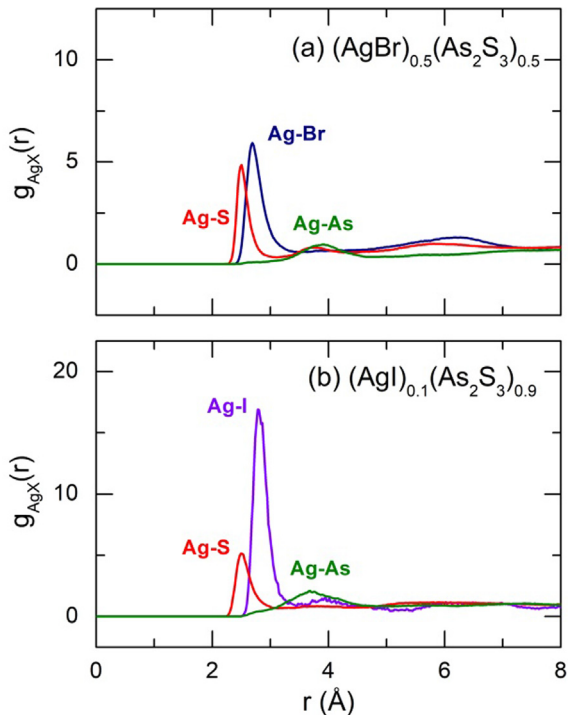


Fig. 16. Ag-related partial pair-distribution functions $g_{\text{AgX}}(r)$ in (a) $(\text{AgBr})_{0.5}(\text{As}_2\text{S}_3)_{0.5}$ and (b) $(\text{AgI})_{0.1}(\text{As}_2\text{S}_3)_{0.9}$ glasses.

of the intermediate range order in both triclinic and monoclinic polymorphs of As_2S_3 [83,84].

The rings statistics of the glass network changes dramatically on alloying with 10 mol.% of AgI, Fig. 18(b). The fraction of rings with homopolar bonds increases by a factor of 8 consistent with the enhanced chemical disorder in $(\text{AgI})_{0.1}(\text{As}_2\text{S}_3)_{0.9}$. The total number of rings normalized to the size of the simulation box, $\sum R_c(p+q)$, remains essentially invariant but the fraction of big rings has decreased substantially. In contrast, the population of small rings has even increased caused by a large number of odd-membered units. Silver-rich $(\text{AgBr})_{0.5}(\text{As}_2\text{S}_3)_{0.5}$ exhibits further evolution. The total number of rings has decreased by a factor of 2 both for small and big ring sizes $p+q$. The compositional changes in ring statistics and FSDP parameters are similar. The essentially invariant FSDP position $Q_0(x)$ correlates with the size of the most populated small rings. The FSDP amplitude reflects

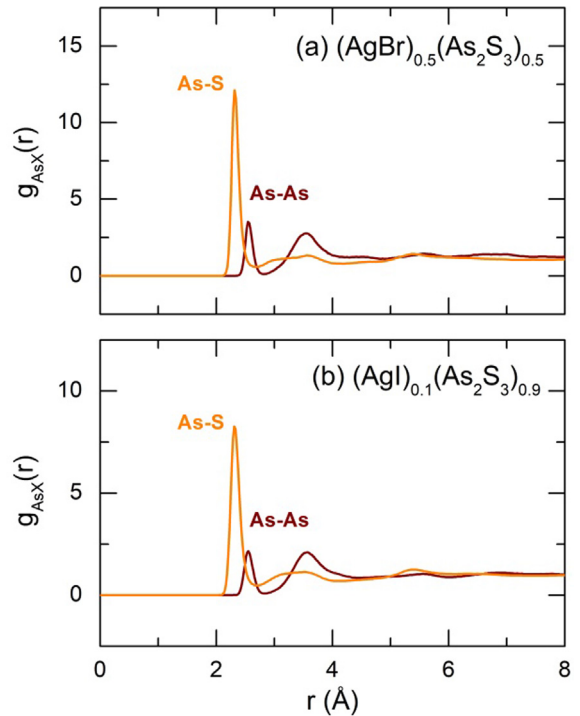


Fig. 17. As-related partial pair-distribution functions $g_{\text{AsX}}(r)$ in (a) $(\text{AgBr})_{0.5}(\text{As}_2\text{S}_3)_{0.5}$ and (b) $(\text{AgI})_{0.1}(\text{As}_2\text{S}_3)_{0.9}$ glasses.

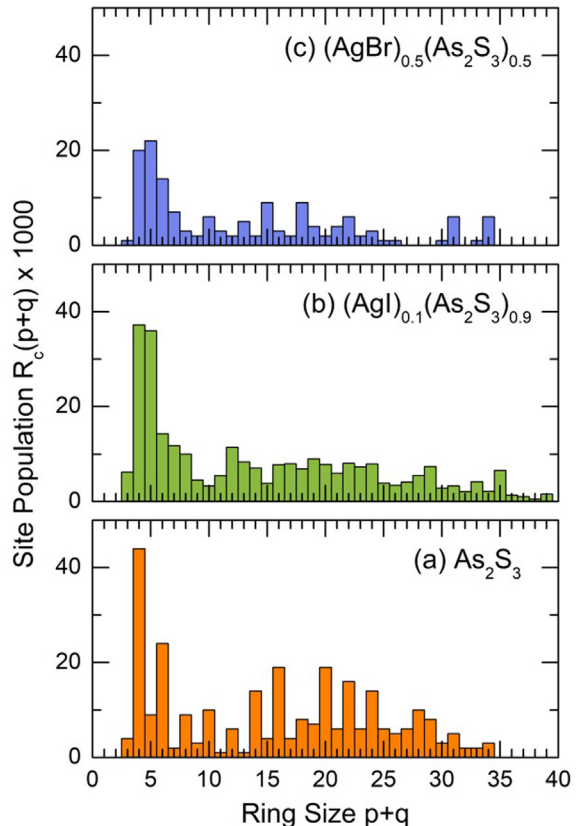


Fig. 18. Ring statistics in glassy (a) As_2S_3 , (b) $(\text{AgI})_{0.1}(\text{As}_2\text{S}_3)_{0.9}$, and (c) $(\text{AgBr})_{0.5}(\text{As}_2\text{S}_3)_{0.5}$.

the population of small rings. In addition, the Raman spectrum of glassy $(\text{AgBr})_{0.5}(\text{As}_2\text{S}_3)_{0.5}$ also reveals the presence of small rings in the glass network. We should also note that the ring statistics

and FSDP evolution are similar to those in $(\text{Na}_2\text{S})_x(\text{As}_2\text{S}_3)_{1-x}$ glasses [85].

3.5. Structural role of silver halides in chalcogenide networks

The diffraction and Raman spectroscopy results supported by FPMD modeling show unexpected structural role of silver halides in thioarsenate glass network. In contrast to common point of view considering AgY additions to be chemically inert and mostly providing the network expansion related to a large size of halide anions [7], we observe a different phenomenon. First, silver halides interact with sulfur species of the host network. As a result, the mixed silver environment is formed. Chemical interaction of silver and sulfur has several consequences. (1) The continuous glass network will be broken similarly to that on modifier additions, e.g. Ag_2S . The fragmented network will be characterized by progressively diminished glass transition temperature T_g , and the composition dependences of T_g for AgY- and $\text{Ag}_2\text{S}-\text{As}_2\text{S}_3$ glasses really exhibit similar trends [10], Figure S6 (Supplementary material). (2) The network fragmentation will also be accompanied by structural changes on the intermediate-range scale. The compositional changes in the FSDP position and amplitude for the studied AgY- As_2S_3 glasses, Fig. 8, as well as the Raman spectra of AgY-rich compositions, show a clear similarity compared to silver thioarsenate glasses $\text{Ag}_2\text{S}-\text{As}_2\text{S}_3$. On the other hand, the enhanced chemical disorder in the $(\text{AgY})_x(\text{As}_2\text{S}_3)_{1-x}$ glasses with increasing x is a consequence of different chemical nature of silver halides and silver sulfide. The Ag_2S modifier, while transforming the bridging sulfur into the terminal one, compensates the sulfur deficiency releasing its own sulfur species. In case of AgY, this possibility is intrinsically missing leading to a chemical bonding rearrangement and the formation of As-As homopolar bonds. Both the Raman spectra and the diffraction data are consistent with this scenario. Resuming, we suggest that both silver halides and possibly alkali and group 11 halides all behave in a similar manner acting as unconventional modifiers.

3.6. Silver distribution as a function of AgY content

Silver distribution and stoichiometry of the mixed silver environment depends on AgY content. The silver-poor glass $(\text{AgI})_{0.1}-(\text{As}_2\text{S}_3)_{0.9}$ belong to the critical percolation domain, which is characterized by a random silver distribution [2,4]. The diffraction data and FPMD modelling confirms a monomeric nature of AgI molecules in the critical percolation region. The shortest Ag-Ag separation distance is centered at $\approx 6 \text{ \AA}$ although a small number of Ag-Ag contacts were observed down to $\approx 4.5 \text{ \AA}$, see a single count of this type in Figure S7 (Supplementary material) and statistically averaged $g_{\text{AgAg}}(r)$, Fig. 15(a). Basically, this indicates the absence of direct Ag-Ag second neighbor contacts and the absence of preferential conduction pathways, ensuring specific ion transport properties and a monotonic decrease of the Haven ratio H_R from $H_R = 1$ as a function of reciprocal Ag-Ag distance.

The silver-rich glass, $(\text{AgBr})_{0.5}(\text{As}_2\text{S}_3)_{0.5}$, belongs to the modifier-controlled region, characterized by a non-random silver distribution and high ionic conductivity related to preferential conduction pathways. The average 2:2 stoichiometry, i.e., 2 sulfur + 2 Br first neighbors for each Ag cation implies at least Ag-related chains or 2D/3D pathways composed of edge- and corner-sharing ES/CS- AgBr_2S_2 tetrahedra. The bimodal silver distribution with the first maximum at the Ag-Ag distance of 3 \AA and the second one at $\approx 4 \text{ \AA}$ is a characteristic feature of the preferential conduction pathways in silver-rich AgY- As_2S_3 glasses. The Haven ratio in these glasses is essentially invariant and low, e.g. $H_R \approx 0.4$, reflecting strongly correlated ion motion within highly connected conduction

pathways. Similar changes in stoichiometry of the mixed silver or copper environment were reported for crystalline MY – A_4X_m compounds with increasing MY content [68–70].

4. Conclusions

Raman spectroscopy, neutron and high-energy X-ray diffraction results supported by FPMD modeling show unexpected and previously unknown structural role of silver halides in two contrasting pseudo-binary systems: $(\text{AgI})_{0.1}(\text{As}_2\text{S}_3)_{0.9}$, belonging to the critical percolation domain, and $(\text{AgBr})_{0.5}(\text{As}_2\text{S}_3)_{0.5}$, from the modifier-controlled region. In a remarkable contrast to a widely accepted point of view suggesting that silver halides are chemically inert dopant salts in a disordered network, providing additional free volume for fast ion migration, we have found that silver halides behave as unconventional modifiers in the AgY- As_2S_3 glasses. Chemical interactions with sulfur species of the glassy host have usual consequences as fragmentation of the continuous network and the appearance of terminal sulfur. Compared to traditional modifiers as Ag_2S , silver halide additions trigger the enhanced chemical disorder, that is, the As-As homopolar bonds for 16% of arsenic species, related to missing sulfur in AgY. The stoichiometry of the mixed silver environment depends on the silver halide content. In the AgI-poor glass, the main structural motif consists of monomeric AgI entities. The tetrahedral local silver environment of isolated silver sites is completed by sulfur. In the superionic AgBr-rich vitreous alloy, the preferential conduction pathways are formed by highly connected edge- and corner-sharing ES/CS- AgBr_2S_2 tetrahedra. The observed structural features are consistent with ionic conductivity and tracer diffusion results. A deep insight into the short- and intermediate range order of the last promising thermoelectric materials can also be used to guide the rational design of thermal transport management, improving the figure of merit ZT .

Declaration of Competing Interest

The authors declare that they have no known competing financial interests or personal relationships that could have appeared to influence the work reported in this paper.

Appendix A. Supplementary data

Supplementary data to this article can be found online at <https://doi.org/10.1016/j.matdes.2022.110547>.

References

- [1] A. Pradel, M. Ribes, Ionic conductivity of chalcogenide glasses, in: J.-L. Adam, X. Zhang (Eds.), Chalcogenide Glasses: Preparation, Properties and Applications, Woodhead, Cambridge, 2014, pp. 169–208.
- [2] E. Bychkov, Superionic and ion-conducting chalcogenide glasses: Transport regimes and structural features, Solid State Ionics 180 (6–8) (2009) 510–516.
- [3] A. Hayashi, N. Masuzawa, S. Yubuchi, F. Tsuji, C. Hotehama, A. Sakuda, M. Tatsumisago, A sodium-ion sulfide solid electrolyte with unprecedented conductivity at room temperature, Nat. Commun. 10 (2019) 5266.
- [4] I. Alekseev, D. Fontanari, A. Sokolov, M. Bokova, M. Kassem, E. Bychkov, Ionic conductivity and tracer diffusion in glassy chalcogenides, in: A.V. Kolobov, K. Shimakawa (Eds.), World Scientific Reference of Amorphous Materials, Vol. 1, World Scientific, Singapore, 2021, pp. 203–249.
- [5] A. Morvan, E. Lavanant, L. Arnoldi, X. Sauvage, L. Calvez, A. Vella, A. Saiter-Fourcine, Nanoscale crystallization mechanisms in a GeSSbCsCl glass ceramic and relationships with mechanical and optical properties, J. Phys. Chem. C 125 (7) (2021) 4196–4204.
- [6] C. Fourmentin, X.-H. Zhang, E. Lavanant, T. Pain, M. Rozé, Y. Guimond, F. Gouttefangeas, L. Calvez, IR GRIN lenses prepared by ionic exchange in chalcohalide glasses, Sci. Reports 11 (2021) 11081.
- [7] J. Swenson, L. Börjesson, Correlation between free volume and ionic conductivity in fast ion conducting glasses, Phys. Rev. Lett. 77 (17) (1996) 3569–3572.

- [8] J. Ren, H. Eckert, Anion distribution in superionic Ag_3PO_4 - Agl glasses revealed by dipolar solid-state NMR, *J. Phys. Chem. C* 117 (2013) 24746–24751.
- [9] C. Renard, G. Coquet, E. Bychkov, Superionic $\text{Agl}-\text{Ml}_n-\text{Sb}_2\text{S}_3$ glasses ($M = \text{Pb}, \text{Sb}$): conduction pathways associated with additional metal iodide, *Solid State Ionics* 154–155 (2002) 749–757.
- [10] R. Zaiter, Silver and/or Mercury Doped Thioarsenate and Thiogermanate Glasses: Transport, Structure, and Ionic Sensitivity, Université du Littoral, France, 2018. Ph.D. Thesis.
- [11] T. Usuki, S. Saito, K. Nakajima, O. Uemura, Y. Kameda, T. Kamiyama, M. Sakurai, Structural and electrical properties of Agl dispersed As-chalcogenide glasses, *J. Non-Cryst. Solids* 312–314 (2002) 570–574.
- [12] Y. Onodera, T. Furukawa, S. Hashimoto, T. Usuki, Y. Amo, Y. Kameda, Vitrification and transport properties in AgBr -doped chalcogenide systems, *Solid State Ionics* 177 (26–32) (2006) 2597–2599.
- [13] I. Alekseev, M. Kassem, M. Fourmentin, D. Le Coq, R. Iizawa, T. Usuki, E. Bychkov, Ionic and electronic transport in $\text{Agl}-\text{As}_2\text{Te}_3$ glasses, *Solid State Ionics* 253 (2013) 181–184.
- [14] E. Bychkov, A. Pradel, M. Ribes, Percolation transition in Ag-doped chalcogenide glasses: comparison of classical percolation and dynamic structure models, *Solid State Ionics* 113–115 (1998) 691–695.
- [15] E. Bychkov, D.L. Price, Neutron diffraction studies of $\text{Ag}_2\text{S}-\text{As}_2\text{S}_3$ glasses in the percolation and modifier-controlled domains, *Solid State Ionics* 136–137 (2000) 1041–1048.
- [16] E. Bychkov, D.L. Price, A. Lapp, Universal trend of the Haven ratio in glasses: origin and structural evidence from neutron diffraction and small-angle neutron scattering, *J. Non-Cryst. Solids* 293–295 (2001) 211–219.
- [17] J. Rupprecht, Silver and copper halide doped $\text{Bi}_2\text{Te}_3-\text{As}_2\text{Se}_3$ thermoelectric material, U.S. Patent 3,258,427 (1966).
- [18] N. Eckstein, T. Nilges, R. Decourt, J.-L. Bobet, B. Chevalier, Effects of partial anion substitution on the thermoelectric properties of silver(I) chalcogenide halides in the system $\text{Ag}_5\text{Q}_2\text{X}$ with $\text{Q} = \text{Te}, \text{Se}$ and S and $\text{X} = \text{Br}$ and Cl , *J. Solid State Chem.* 184 (4) (2011) 778–785.
- [19] (a) Y. Xia, V. I. Hegde, K. Pal, X. Hua, D. Gaines, S. Patel, J. He, M. Aykol, C. Wolverton, High-throughput study of lattice thermal conductivity in binary rocksalt and zinc blende compounds including higher-order anharmonicity, *Phys. Rev. X* 10 (2020) 041029; (b) X. Yang, Z. Dai, Y. Zhao, S. Meng, Superhigh thermoelectric figure of merit in silver halides AgCl and AgBr from first principles, arXiv:1904.06010.
- [20] C. Künzel, K. Dammmer, U. Betke, J. Urbaschok, F. Scheffler, High-performance doctor bladed thermoelectric microlayers, *Mater. Design* 196 (2020) 109087.
- [21] J. Xu, Y. Hu, X. Zhu, Crystallization and electrical conversion behavior of $\text{Ge}_1\text{Sb}_9/\text{HfO}_2$ superlattice-like phase change films, *Mater. Design* 208 (2021) 109913.
- [22] G. D'Arrigo, M. Scuderi, A. Mio, G. Favaro, M. Conte, A. Sciuto, M. Buscema, G. Li-Destri, E. Carria, D. Mello, M. Calabretta, A. Sitta, J. Pries, E. Rimini, Mechanical characterization and properties of continuous wave laser irradiated $\text{Ge}_2\text{Sb}_2\text{Te}_3$ stripes, *Mater. Design* 202 (2021) 109545.
- [23] J. He, L. Zhang, L. Liu, Improving thermal conduction across cathode/electrolyte interfaces in solid-state lithium-ion batteries by hierarchical hydrogen-bond network, *Mater. Design* 194 (2020) 108927.
- [24] R. Song, N. Zhang, H. Dong, P. Wang, H. Ding, J. Wang, S. Li, Self-standing three-dimensional porous NiO/Ni anode materials for high-areal capacity lithium storage, *Mater. Design* 215 (2022) 110448.
- [25] W. Zhong, Y. Liu, X. Yang, C. Wang, W. Xin, Y. Li, W. Liu, H. Xu, Suspended few-layer GaS photodetector with sensitive fast response, *Mater. Design* 212 (2021) 110233.
- [26] J. Su, X. Wang, C. Shao, Y. Guo, L. Xian, Strain-controlled Rashba spin-orbit coupling effect in SnS and SnSe monolayers, *Mater. Design* 209 (2021) 110005.
- [27] A.C. Hannon, W.S. Howells, A.K. Soper, ATLAS: A suite of programs for the analysis of time-of-flight neutron diffraction data from liquid and amorphous samples, *Inst. Phys. Conf. Ser.* 107 (1990) 193–211.
- [28] A.P. Hammersley, S.O. Svensson, M. Hanfland, A.N. Fitch, D. Häusermann, Two-dimensional detector software: From real detector to idealised image or two-theta scan, *High Pressure Res.* 14 (1996) 235–248.
- [29] L.B. Skinner, C.J. Benmore, J.B. Parise, Area detector corrections for high quality synchrotron X-ray structure factor measurements, *Nucl. Instrum. Methods A* 662 (2012) 61–70.
- [30] T.D. Kühne, M. Iannuzzi, M. Del Ben, V.V. Rybkin, P. Seewald, F. Stein, T. Laino, R.Z. Khalilullin, O. Schütt, F. Schiffmann, D. Golze, J. Wilhelm, S. Chulkov, M.H. Bani-Hashemian, V. Weber, U. Borštník, M. Taillefumier, A.S. Jakobovits, A. Lazzaro, H. Pabst, T. Müller, R. Schade, M. Guidon, S. Andermatt, N. Holmberg, G.K. Schenter, A. Hehn, A. Bussy, F. Belleflamme, G. Tabacchi, A. Glöß, M. Lass, I. Bethune, C.J. Mundy, C. Plessl, M. Watkins, J. Vandevondele, M. Krack, J. Hutter, CP2K: An electronic structure and molecular dynamics software package - Quickstep: Efficient and accurate electronic structure calculations, *J. Chem. Phys.* 152 (2020) 194103.
- [31] J.P. Perdew, A. Ruzsinszky, G.I. Csonka, O.A. Vydrov, G.E. Scuseria, L.A. Constantin, X. Zhou, K. Burke, Restoring the density-gradient expansion for exchange in solids and surfaces, *Phys. Rev. Lett.* 100 (2008) 136406.
- [32] J. Akola, P. Jóvári, I. Voleská, J. Kolář, T. Wágner, R.O. Jones, Structure, electronic, and vibrational properties of amorphous As_2 and AgAs_2 : Experimentally constrained density functional study, *Phys. Rev. B* 89 (2014) 064202.
- [33] T. Ohkubo, K. Ohara, E. Tsuchida, Conduction mechanism in $70\text{Li}_2\text{S}-30\text{P}_2\text{S}_5$ glass by ab initio molecular dynamics simulations: comparison with $\text{Li}_7\text{P}_3\text{S}_{11}$ crystal, *ACS Appl. Mater. Interfaces* 12 (23) (2020) 25736–25747.
- [34] S. Kohara, M. Shiga, Y. Onodera, H. Masai, A. Hirata, M. Murakami, T. Morishita, K. Kimura, K. Hayashi, Relationship between diffraction peak, network topology, and amorphous-forming ability in silicon and silica, *Sci. Reports* 11 (2021) 22180.
- [35] O. Gereben, P. Jóvári, L. Temleitner, L. Pusztai, A new version of the RMC++ Reverse Monte Carlo programme, aimed at investigating the structure of covalent glasses, *J. Optoelectr. Adv. Mater.* 9 (2007) 3021–3027.
- [36] S. Nosé, A molecular dynamics method for simulations in the canonical ensemble, *Mol. Phys.* 52 (1984) 255–268.
- [37] W.G. Hoover, Canonical dynamics: equilibrium phase-space distributions, *Phys. Rev. A* 31 (1985) 1695–1697.
- [38] A. Tverjanovich, M. Khomenko, C.J. Benmore, M. Bokova, A. Sokolov, D. Fontanari, M. Kassem, T. Usuki, E. Bychkov, Bulk glassy GeTe_2 : a missing member of the tetrahedral Ge_xTe_2 family and a precursor for the next generation of phase-change materials, *Chem. Mater.* 33 (2021) 1031–1045.
- [39] M. Bokova, A. Tverjanovich, C.J. Benmore, D. Fontanari, A. Sokolov, M. Khomenko, M. Kassem, I. Ozheredov, E. Bychkov, Unraveling the atomic structure of bulk binary Ga-Te glasses with surprising nanotectonic features for phase-change memory applications, *ACS Appl. Mater. Interfaces* 13 (31) (2021) 37363–37379.
- [40] A. Tverjanovich, M. Khomenko, C.J. Benmore, S. Bereznev, A. Sokolov, D. Fontanari, A. Kiselev, A. Lotin, E. Bychkov, Atypical phase-change alloy Ga_2Te_3 : atomic structure, incipient nanotectonic nuclei, and multilevel writing, *J. Mater. Chem. C* 9 (2021) 17019–17032.
- [41] YOJI Kawamoto, NAGAO Nagura, SHOJI Tsuchihashi, Properties of Ag-containing sulfide glasses, *J. Am. Ceram. Soc.* 56 (5) (1973) 289–290.
- [42] A. Piarristeguy, M. Ramonda, N. Kuwata, A. Pradel, M. Ribes, Microstructure of $\text{Ag}_2\text{S}-\text{As}_2\text{S}_3$ glasses, *Solid State Ionics* 177 (35–36) (2006) 3157–3160.
- [43] P. Debye, A.M. Bueche, Scattering by an inhomogeneous solid, *J. Appl. Phys.* 20 (6) (1949) 518–525.
- [44] P. Armand, A. Ibanez, E. Philippot, C. Williams, D. Bittencourt, Small angle X-ray scattering and the structure of Ge-S and $\text{Ge}_2\text{S}_2-\text{Ag}_2\text{S}$ glassy systems, *J. Phys. IV Coll.* 3 (1993). C8–389–C8–392.
- [45] E. Bychkov, M. Miloshova, D.L. Price, C.J. Benmore, A. Lorriau, Short, intermediate and mesoscopic range order in sulfur-rich binary glasses, *J. Non-Cryst. Solids* 352 (1) (2006) 63–70.
- [46] T. Li, A.J. Senesi, B. Lee, Small angle X-ray scattering for nanoparticle research, *Chem. Rev.* 116 (18) (2016) 11128–11180.
- [47] S. Hany, M. Milochova, K. Littrell, R. Lorange, J.-B. Vogt, E. Abi-Aad, E. Bychkov, Advanced characterization of cryogenic 9Ni steel using synchrotron radiation, neutron scattering and ^{57}Fe Mössbauer spectroscopy, *Mater. Design* 146 (2018) 219–227.
- [48] X. Han, H. Tao, R. Pa, Y. Lang, C. Shang, X. Xing, Q. Tu, X. Zhao, Structure and vibrational modes of As-S-Se glasses: Raman scattering and ab initio calculations, *Phys. Proc.* 48 (2013) 59–64.
- [49] M. Kassem, M. Bokova, A.S. Tverjanovich, D. Fontanari, D. Le Coq, A. Sokolov, P. Masselin, S. Kohara, T. Usuki, A.C. Hannon, C.J. Benmore, E. Bychkov, Bent HgI_2 molecules in the melt and sulfide glasses: Implications for nonlinear optics, *Chem. Mater.* 31 (2019) 4103–4112.
- [50] G. Štrbac, S.R. Lukic-Petrović, D. Štrbac, V. Benešou, A. Chrissanthopoulos, S.N. Yannopoulos, Optical properties and structure of As/Sb chalcogenide glasses by Raman scattering and DFT calculations, *J. Phys. Chem. B* 124 (2020) 2950–2960.
- [51] A. Bertoluzzo, C. Fagnano, P. Monti, G. Semerano, Raman and infrared spectra of As_2S_x chalcogenide glasses with $x \leq 3$, *J. Non-Cryst. Solids* 29 (1) (1978) 49–60.
- [52] P.J.S. Ewen, A.E. Owen, Resonance Raman scattering in As-S glasses, *J. Non-Cryst. Solids* 35–36 (1980) 1191–1196.
- [53] K. Tanaka, Chemical and medium-range orders in As_2S_3 glass, *Phys. Rev. B* 36 (1987) 9746–9752.
- [54] D.G. Georgiev, P. Boolchand, K.A. Jackson, Intrinsic nanoscale phase separation of bulk As_2S_3 glass, *Phil. Mag.* 83 (25) (2003) 2941–2953.
- [55] V.V. Brazhkin, A.G. Gavrilyuk, A.G. Lyapin, Y.A. Timofeev, Y. Katayama, S. Kohara, AsS : Bulk inorganic molecular based inorganic chalcogenide glass, *Appl. Phys. Lett.* 91 (2007) 031912.
- [56] S. Kharbishi, Spectral-structural characteristics of the extremely scarce silver arsenic sulfosalts, proustite, smithite, trechmannite and xanthoconite: μ -Raman spectroscopy evidence, *Spectrochim. Acta A* 177 (2017) 104–110.
- [57] T. Wágner, V. Peřina, A. Macková, E. Rauhala, A. Seppälä, M. Vlček, S.O. Kasap, M. Vlček, M. Frumar, The tailoring of the composition of Ag-As-S amorphous films using photo-induced solid state reaction between Ag and $\text{As}_{30}\text{S}_{70}$ films, *Solid State Ionics* 141–142 (2001) 387–395.
- [58] M. Krbal, T. Wagner, T. Srba, J. Schwarz, J. Orava, T. Kohoutek, V. Zima, L. Benes, S.O. Kasap, M. Frumar, Properties and structure of $\text{Ag}_x(\text{As}_{0.33}\text{S}_{0.67})_{100-x}$ bulk glasses, *J. Non-Cryst. Solids* 353 (13–15) (2007) 1232–1237.
- [59] E. Hellner, H. Burzlaff, Die Struktur des Smithits AgAsS_2 , *Naturwissenschaften* 51 (2) (1964) 35–36.
- [60] T. Matsumoto, W. Nowacki, The crystal structure of trechmannite, AgAsS_2 , *Z. Kristallogr.* 129 (1–4) (1969) 163–177.
- [61] P. Engel, W. Nowacki, Die Kristallstruktur von Ag_3AsS_3 , *Acta Crystallogr. B* 24 (1968) 77–81.
- [62] S. Allen, Phase transitions in proustite, Structural studies, *Phase Trans.* 6 (1985) 1–24.
- [63] I. Petri, P.S. Salmon, H.E. Fischer, Defects in a disordered world: the structure of glassy GeSe_2 , *Phys. Rev. Lett.* 84 (2000) 2413–2416.

- [64] W. Zhou, D.E. Sayers, M.A. Paesler, B. Boucher-Fabre, Q. Ma, D. Raoux, Structure and photoinduced structural changes in a-As₂S₃ films: a study by differential anomalous X-ray scattering, *Phys. Rev. B* 47 (1993) 686–694.
- [65] S. Tahara, H. Ueno, K. Ohara, Y. Kawakita, S. Kohara, S. Ohno, S. Takeda, Medium-range correlation of Ag ions in superionic melts of Ag₂Se and AgI by reverse Monte Carlo structural modelling—connectivity and void distribution, *J. Phys.: Condens. 23* (23) (2011) 235102, <https://doi.org/10.1088/0953-8984/23/23/235102>.
- [66] R. Zaiter, M. Kassem, D. Fontanari, A. Cuisset, C.J. Benmore, E. Bychkov, Ionic transport and atomic structure of AgI-HgS-GeS₂ glasses, *Pure Appl. Chem.* 91 (11) (2019) 1807–1820.
- [67] I.T. Penfold, P.S. Salmon, Glass formation and short-range order in chalcogenide materials: the (Ag₂₅)x(As₂₅S₃)_{1-x} (0 ≤ x ≤ 1) pseudobinary tie line, *Phys. Rev. Lett.* 64 (1990) 2164–2167.
- [68] A. Pfitzner, S. Reiser, H.-J. Deiseroth, (CuI)P₄Se₄: an adduct of polymeric P₄Se₄ with CuI, *Z. Anorg. Allg. Chem.* 625 (1999) 2196–2201.
- [69] H.-J. Deiseroth, M. Wagener, E. Neumann, (AgI)₂Te₆ and (AgI)₂Se₆: new composite materials with cyclic Te₆ and Se₆ molecules stabilized in the “solid solvent” AgI, *Eur. J. Inorg. Chem.* 2004 (2004) 4755–4758.
- [70] A. Biegerl, E. Brunner, C. Gröger, M. Scheer, J. Wachter, M. Zabel, The unexpected versatility of P₄S₃ as a building block in polymeric copper halide networks: 2,3-P, 1,2,3-P and all-P coordination, *Chem. Eur. J.* 13 (2007) 9270–9276.
- [71] P.M. Smith, A.J. Leadbetter, A.J. Apling, The structures of orthorhombic and vitreous arsenic, *Phil. Mag.* 31 (1) (1975) 57–64.
- [72] S. Soyer-Uzun, S. Sen, B.G. Aitken, Network vs molecular structural characteristics of Ge-doped arsenic sulfide glasses: a combined neutron/X-ray diffraction, extended X-ray absorption fine structure, and Raman spectroscopic study, *J. Phys. Chem. C* 113 (2009) 6231–6242.
- [73] A. Di Cicco, M. Taglienti, M. Minicucci, A. Filippone, Local structure of liquid and solid silver halides probed by XAFS, *J. Synchrotron Rad.* 8 (2) (2001) 761–763.
- [74] Y. Onodera, T. Usuki, T. Nasu, S. Kohara, Structure of silver bromide doped chalcogenide glasses, *Solid State Ionics* 262 (2014) 469–471.
- [75] P.S. Salmon, S. Xin, H.E. Fischer, Structure of the glassy fast ion conductor AgPS₃ by neutron diffraction, *Phys. Rev. B* 58 (1998) 6115–6123.
- [76] J. Kalikka, J. Akola, R.O. Jones, S. Kohara, T. Usuki, Amorphous Ge₁₅Te₈₅: Density functional, high-energy X-ray and neutron diffraction study, *J. Phys.: Condens. 24* (Matter 2012.) 015802.
- [77] T. Aschebrock, S. Kümmel, Ultranonlocality and accurate band gaps from a meta-generalized gradient approximation, *Phys. Rev. Res.* 1 (2019) 033082.
- [78] D. Dragoni, M. Bernasconi, Structural and electronic properties of liquid, amorphous and supercooled liquid phases of In₂Te₅ from first-principles, *J. Chem. Phys.* 151 (2019) 134503.
- [79] G. Delaizir, A. Piarristeguy, A. Pradel, O. Masson, A. Bouzid, Short range order and network connectivity in amorphous AsTe₃: a first principles, machine learning, and XRD study, *CCCP* 22 (2020) 24895–24906.
- [80] A. Bouzid, T.-L. Pham, Z. Chaker, M. Boero, C. Massobrio, Y.-H. Shin, G. Ori, Quantitative assessment of the structure of Ge₂₀Te₇₃I₇ chalcohalide glass by first-principles molecular dynamics, *Phys. Rev. B* 103 (2021) 094204.
- [81] S. Le Roux, P. Jund, Ring statistics analysis of topological networks: new approach and application to amorphous GeS₂ and SiO₂ systems, *Comput. Mater. Sci.* 49 (2010) 70–83.
- [82] S.I. Simdyankin, S.R. Elliott, Z. Hajnal, T.A. Niehaus, T.h. Frauenheim, Simulation of physical properties of the chalcogenide glass As₂S₃ using a density-functional-based tight-binding method, *Phys. Rev. B* 69 (2004) 144202.
- [83] D.J.E. Mullen, W. Nowacki, Refinement of the crystal structures of realgar, AsS and orpiment, As₂S₃, *Z. Kristallogr.* 136 (1972) 48–65.
- [84] A.R. Kampf, R.T. Downs, R.M. Housley, R.A. Jenkins, J. Hyršl, Anorpiment, As₂S₃, the triclinic dimorph of orpiment, *Mineralog. Mag.* 75 (6) (2011) 2857–2867.
- [85] M. Kassem, T. Bounazef, D. Fontanari, A. Sokolov, M. Bokova, A.C. Hannon, E. Bychkov, Chemical and structural variety in sodium thioarsenate glasses studied by neutron diffraction and supported by first-principles simulations, *Inorg. Chem.* 59 (22) (2020) 16410–16420.